Supercell Collision with Sea-Breeze Flows of Different Depths and Intensities: Dynamic and Thermodynamic Responses

RUQIAN ZHANG[a] AND MING XUE[b]

[a] *Key Laboratory of Mesoscale Severe Weather, Ministry of Education, School of Atmospheric Sciences, Nanjing University, Nanjing, Jiangsu, China*

[b] *Center for Analysis and Prediction of Storms and School of Meteorology, University of Oklahoma, Norman, Oklahoma*

(Manuscript received 11 November 2025, in final form 1 September 2026, accepted 23 September 2026)

ABSTRACT: Studies on how sea breezes affect the development of coastal supercell thunderstorms remain limited. Idealized simulations are conducted to investigate how sea-breeze flows driven by a cold marine boundary layer (CMBL) of varying initial strengths (−3 and −5 K) and depths (500 and 1500 m) influence supercell evolution. Deep and shallow CMBL air exerts different influences on supercell development. During the early stage, when a deep-sea-breeze front initiated by a 1500-m-deep CMBL collides with the supercell, the upward dynamic vertical perturbation pressure gradient force (DVPPGF) associated with low-level flow convergence/deformation is larger than that in the control simulation without CMBL (CTRL). During the later stage, after the deep-sea-breeze front has passed underneath the supercell, the persistent flow behind the front leads to a significant increase in both 0–1-km storm-relative helicity and 2–5-km updraft helicity in deep CMBL cases, and the updraft is accompanied by a larger rotation-induced DVPPGF. These effects result in stronger low-level upward DVPPGF in both stages for deep CMBL cases compared with CTRL, enabling the DVPPGF to compensate for the reduced effective buoyancy (EB) caused by the colder sea-breeze air, resulting in the ingestion of substantially more inflow parcels, and a larger area of strong updraft, greater total condensate mass, and increased precipitation. Storm characteristics in shallow CMBL cases are similar to those of CTRL. Effects of CMBL are independent of the level at which maximum convective available potential energy occurs at ~1 km or near the surface in the sounding.

KEYWORDS: Convective storms/systems; Updrafts/downdrafts; Sea breezes; Supercells

1. Introduction

Globally, around 40% of the world's population resides in coastal regions (United Nations 2017), and roughly half of this population is affected by coastal precipitation (Bergemann et al. 2015). Such regions are prone to heavy rainfall from convective systems, which are commonly intensified by the sea-breeze flows. The sea-breeze flow is a common phenomenon in coastal regions. During the daytime, the temperature contrast between the warmer land surface and the cooler adjacent ocean drives the development of sea-breeze flows. Chen et al. (2016) investigated the diurnal variations of land and sea breezes and their associated precipitation over the South China coastal region during the mei-yu season. Their results show that, during the daytime, a rainfall band begins to develop along the onshore side of the coastline around noon and subsequently propagates inland. This progression is closely linked to the inland penetration of the sea-breeze flow. Lombardo and Kading (2018) show that enhanced precipitation occurs just prior to the collision between a squall line and the deepest sea-breeze flow. The squall line modifies the environment downstream by promoting the formation of a moist absolutely unstable layer (MAUL) and lowering the level of free convection (LFC) to below the top of the deepest sea-breeze flow. The sea-breeze flow moving into the storm-modified environment successfully lifts air parcels to the reduced LFC, generating convective towers ahead of the squall line. Many studies have focused on the role of the sea breeze in convective initiation, the development of shallow convective clouds, and the organization of deep convection such as squall lines (e.g., Dailey and Fovell 1999; Yu and Hsieh 2009; Fu et al. 2022; Wu and Lombardo 2024; Boyer et al. 2025), but relatively few studies have investigated the impact of sea breeze on coastal supercell storms, which are distinguished by their intense, rotating updrafts.

In addition to intense rainfall, coastal supercell thunderstorms are capable of producing a range of severe weather phenomena, including large hail, damaging winds, and, in some cases, tornadoes (Soderholm et al. 2017; Jin et al. 2019; Chan et al. 2022). Coastal supercells occur frequently worldwide, including in eastern China (where ~36% of supercells form within coastal regions; Zhang et al. 2025), the eastern United States (Coffer et al. 2020), and eastern Australia (Hartigan et al. 2021). These high-impact events pose significant threats to both coastal infrastructure and human safety. For example, the 1999 Sydney and 2014 Brisbane high-precipitation, large-hail supercells in Australia each caused more than one billion in damage in Australian dollars (Hartigan et al. 2021). Northern Jiangsu, an east coast province of China, has the highest frequency of tornado occurrence in China (Zhang et al. 2023; Zhang et al. 2025), with the EF4 supercell tornado in Funing, Jiangsu, being an example (Meng et al. 2018; Sun et al. 2019).

As supercells propagate seaward, they may encounter onshore coastal winds, leading to the formation of a pronounced low-level convergence zone, which can enhance storm organization or intensity. Based on idealized simulations, Hartigan et al. (2021) suggest that ambient low-level winds within the

Corresponding author: Ming Xue, mxue@ou.edu

DOI: 10.1175/JAS-D-25-0210.1

© 2026 American Meteorological Society. This published article is licensed under the terms of the default AMS reuse license. For information regarding reuse of this content and general copyright information, consult the AMS Copyright Policy (www.ametsoc.org/PUBSReuseLicenses).

Brought to you by UNIVERSITY OF OKLAHOMA LIBRARY | Unauthenticated | Downloaded 10/27/26 06:31 PM UTC

sea-breeze air mass play a critical role in supercell development by decelerating gust-front propagation and enhancing updraft rotation. However, in Hartigan et al. (2021), the base-state substitution modeling technique was employed to represent the sea-breeze air mass and the simulation of an actual sea-breeze front was excluded, making the study highly idealized. The winds near and behind the sea-breeze front exhibit distinct characteristics, and variations in the frontal position may differently influence supercell development. Further research is needed to better understand the impact of sea-breeze fronts at different inland-progressing stages on the evolution of supercells, particularly the dynamic and thermodynamic processes involved.

Specifying a relatively cold marine boundary layer (CMBL), in the form of a cold block of air overlying the ocean surface, is one commonly used approach to initiate a sea-breeze front in idealized numerical simulations (e.g., Wissmeier et al. 2010; Lombardo and Kading 2018; Chen et al. 2019; Wu and Lombardo 2024). Specifically, Lombardo and Kading (2018) investigated the effects of varying depth and temperature deficit of the CMBL on squall-line development. In their study, the low-level winds associated with the CMBL enhance convergence at the leading edge of cold pool, thereby increasing vertical acceleration of the squall line. In addition, a local temperature deficit is present behind the sea-breeze front generated by the CMBL. The increasingly cold and stable CMBL forces the source of air ingested by the squall line to become more elevated.

A few studies have investigated the influence of a stabilizing boundary layer on supercell evolution. Davenport and Parker (2015) examined dissipating supercells through idealized simulations under conditions of environmental cooling and reduced wind shear achieved through the base-state substitution technique. With these environmental changes, the source regions for updraft parcels become more elevated, and fewer parcels are ingested into the updrafts over time. The reduction in buoyancy acceleration of supercell updrafts is largely consistent with the presence of cooled air, while the decrease in dynamical acceleration is associated with the reduction in shear. Also using the base-state substitution technique, Coffer and Parker (2015) studied the response of a supercell initialized and matured within an afternoon environment to the changed earlier evening environment with increased low-level shear; they found that the increased dynamic pressure lifting associated with the enhanced mesocyclone was able to offset the negative effect of the colder boundary layer air, therefore reducing buoyancy, and the updraft can be stronger in the early evening environment. Although the base-state substitution technique is useful for examining supercell responses to environmental changes, it gradually modifies the base-state vertical profiles throughout the model domain. Consequently, the resulting supercell responses and their underlying physical mechanisms may differ from those associated with colder air approaching from the inflow region and directly interacting with the storm. For these reasons, we perform a set of idealized simulations in which sea-breeze flows resulting from an initially specified pool of CMBL air of two different depths and two different magnitudes of negative potential temperature perturbations progress inland and collide with the mature supercell.

By analyzing and comparing the idealized simulations, and with the help of pressure diagnostic equations decomposing contributions from different terms and processes, this paper aims to address the following questions:

1) How do variations in the sea-breeze intensity (i.e., increases in local wind speed and stability) generated by a CMBL influence the development of supercells?
2) Do different stages of a sea-breeze front intruding into a supercell have distinct effects on its updrafts? If so, what are these effects?
3) What are the dynamic and thermodynamic characteristics of the air feeding the updraft in sea-breeze-influenced supercells?
4) Does the vertical distribution of convective available potential energy (CAPE) in the environmental sounding have a significant impact on the development of a supercell under the influence of a sea-breeze front?

The rest of this paper is organized as follows. Section 2 describes the model setup, the base-state environment of the simulations, the initialization of the supercells and sea-breeze flows, and the diagnostic pressure equations to be used. Section 3 presents the simulation results and discusses the mechanisms of the supercell responses to colliding sea-breeze flows. Section 4 presents the main conclusions.

2. Model and methods

a. *Model setup*

Idealized simulations are conducted using the nonhydrostatic Cloud Model 1 (CM1), version 21 (Bryan and Fritsch 2002). The namelist parameters used are shown in Table 1. The model domain spans 400 km horizontally (from $x/y = -200$ to 200 km) and 18 km vertically. The horizontal grid spacing is 500 m. In the vertical, the grid is stretched from 100 m near the surface to 250 m below 3 km, yielding a total of 80 vertical levels. A free-slip condition is applied at the upper boundary. To better represent a realistic coastal environment, a semislip condition is used at the lower boundary, assuming a wooded-wetland surface over the left half of the domain and a water surface over the right half. Open radiative boundary conditions are specified at the lateral boundaries. Following Lombardo and Kading (2018), microphysical processes are parameterized using the Morrison double-moment scheme (Morrison et al. 2009). Subgrid-scale turbulence is parameterized using a 1.5-order turbulent kinetic energy (TKE) scheme. The advection of velocities and scalars uses the fifth-order horizontal and vertical advection schemes with implicit diffusion (Wicker and Skamarock 2002). A Klemp–Wilhelmson time-splitting, vertically implicit, horizontally explicit vertical velocity–pressure solver is used. To isolate the storm's response to the specified CMBL flow from the effects of time-varying environmental parameters, radiation and surface heat and moisture fluxes are excluded, as in Lombardo and Kading (2018). Simulations are performed for 3 h, with data output recorded every 5 min. The Weisman and Klemp sounding used in this paper is known to produce long-lived supercells, and the 3-h simulation duration was chosen to focus on the

Brought to you by UNIVERSITY OF OKLAHOMA LIBRARY | Unauthenticated | Downloaded 10/27/26 06:31 PM UTC

TABLE 1. Select CM1, release 21.1, and namelist parameters used for simulations.

CM1 namelist parameter	Description	Value(s)
nx, *ny*, *nz*	Number of grid points in *x*, *y*, and *z* directions	800, 800, 80
dx, *dy*, *dz*	Horizontal grid spacing in *x*, *y*, and *z* directions	500, 500, 200 m
stretch_*z*, ztop, str_bot, str_top, dz_bot, dz_top	Vertical grid stretching parameters	2, 18 000, 0, 3000, 100, 250 m
dtl	Large time step	3 s
timax	Maximum integration time	10 800 s
tapfrq	Frequency of 3D model output	300 s
isnd	Base-state sounding	5 (Weisman–Klemp analytic sounding)
iwnd	Base-state wind profile	2 (Weisman–Klemp supercell)
iinit	3D initialization option	1 (warm bubble)
cm1setup	CM1 setup to determine how turbulence is handled	1 (large-eddy simulation)
hadvordrs, vadvordrs, hadvordv, vadvordv	Order of horizontal/vertical advection scheme for scalars and velocities	5, 5, 5, 5
sgsmodel	Subgrid-scale turbulence model for large-eddy simulation	1 (TKE scheme)
irdamp	Use upper-level Rayleigh damping zone?	1 (on)
rdalpha	Rayleigh damping coefficient	0.003 s^{-1}
zd	Height above which Rayleigh damping is applied	15 000 m
wbc, ebc, nbc, sbc	West, east, north, and south lateral boundary conditions	2 (open radiative)
bbc	Bottom boundary conditions for wind	3 (semislip)
tbc	Top boundary conditions for wind	1 (free slip)
initsfc	Initial surface conditions	4 (coastline)
ptype	Microphysics scheme	5 (Morrison double-moment scheme)

direct effects of the collision between the sea-breeze flow and the supercell storm outflow and the subsequent interactions at the mature stage of supercells.

b. *Base-state environment*

Simulations are initialized using the analytic thermodynamic sounding of Weisman and Klemp (1982), modified with a relative humidity (rh) profile scaled by an exponent of 0.75 {rh = 1 − 0.75 × [(*zh*/12)$^{0.75}$]; Fig. 1}. The choice of sounding is consistent with Lombardo and Kading (2018). This sounding yields a surface-based CAPE of 1903 J kg^{-1} and convective inhibition (CIN) of 43 J kg^{-1}. The most unstable CAPE is 2302 J kg^{-1} with a corresponding CIN of only 1.5 J kg^{-1}. The surface-based lifting condensation level (LCL) is 1015 m, and the LFC is at 1531 m. The initial vertical wind profile is the quarter circle plus a constant shear profile described in Weisman and Klemp (1982), shown in the upper-right corner of Fig. 1. Such an environment is known to support supercell storms. The water vapor mixing ratio within CMBL was not modified, as the objective of this study is to isolate the influence of low-level wind and temperature deficit changes induced by the CMBL on supercells.

c. *Supercell and sea-breeze initializations*

All supercells are initiated at $t = 0$ with an elliptical 1-K warm bubble centered at $x = -80$ km, $z = 1.4$ km. The horizontal and vertical radii of the bubble are 10 and 1.4 km, respectively. Warm-bubble perturbations with magnitudes of 2 and 3 K are also tested. Because the sea-breeze interaction occurs during the mature stage of the supercell, the specific warm-bubble magnitude does not have a significant impact on the results. The sea-breeze flow of varying coldness is initialized by specifying a vertically linearly decreasing magnitude of negative potential temperature perturbations θ' up to a depth of h within the CMBL. The distribution θ'_M within the CMBL is as follows:

$$\theta'_M = \theta'_0\left(\frac{h - z}{h}\right), \quad \text{for } z < h. \tag{1}$$

We compare four experiments, CMBL500_3, CMBL500_5, CMBL1500_3, and CMBL1500_5, featuring an initial cold CMBL with $h = 500$ or 1500 m and $\theta'_0 = -3$ or -5 K, against a control supercell simulation (CTRL) without sea-breeze interference. Observed CMBL depths typically range from 200 to 1500 m, and CMBL temperature deficits generally range from −2 to −8 K. The values used in the CMBL experiments fall within these observed ranges and are further supported by idealized numerical simulations (Lombardo and Colle 2013; Lombardo et al. 2016; Lombardo and Kading 2018; Wu and Lombardo 2024). The CMBL is located on the right side of the simulation domain to facilitate the collision between the eastward-moving supercell and the westward-moving sea breeze. The initial position of the CMBL's left boundary varies around $x = 0$ km (from $x = -10$ to 3 km) in the four simulations to ensure that sea-breeze air collides with the cold pool of supercell at roughly the same time across different experiments.

Brought to you by UNIVERSITY OF OKLAHOMA LIBRARY | Unauthenticated | Downloaded 10/27/26 06:31 PM UTC

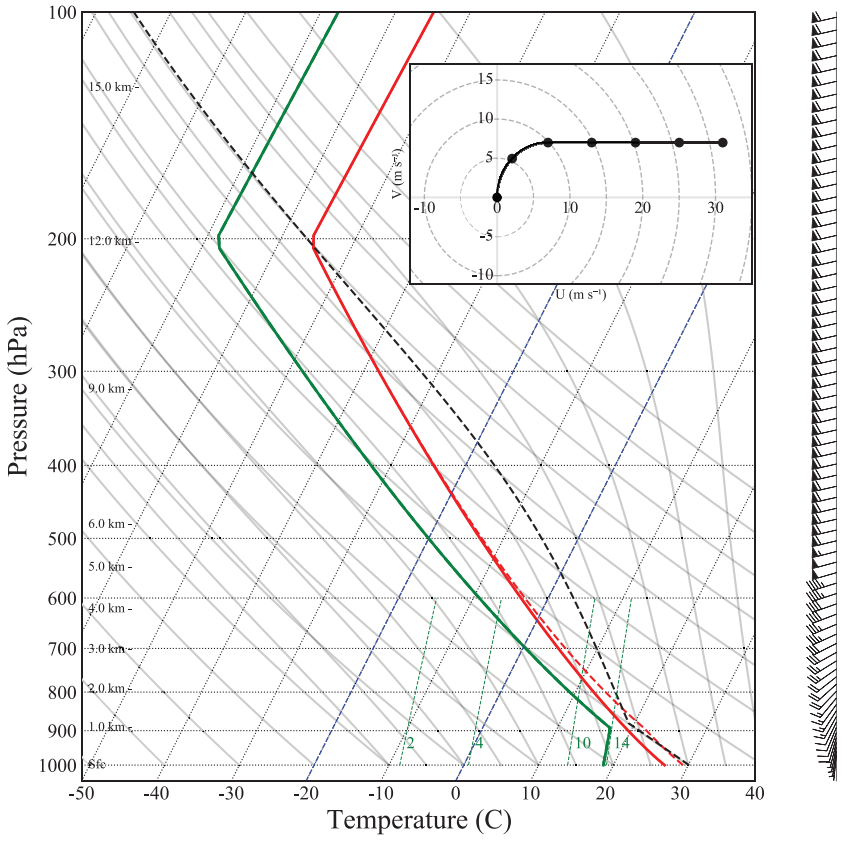


FIG. 1. Initial sounding and hodograph (top-right corner). The solid red, solid green, dashed red, and dashed black lines denote temperature, dewpoint, virtual temperature, and parcel trace. The dashed green line is the revised dewpoint in the boundary layer used in section 3f. The dashed blue lines denote 0° and −20°C isotherms. The thin dashed green lines represent the constant water vapor mixing ratio at 2, 4, 10, and 14 g kg^{-1}. The black line in the hodograph represents the 0–6-km wind profile, with markers every 1 km in height. The dashed circles are isotachs drawn every 5 m s^{-1}.

d. *Vertical momentum equation and perturbation pressure diagnostics*

Lagrangian vertical momentum equation mainly has the vertical perturbation pressure gradient force (VPPGF) and buoyancy terms on its right-hand side:

$$\frac{dw}{dt} = -\frac{1}{\overline{\rho}}\frac{\partial p'}{\partial z} + B, \tag{2}$$

where w is the vertical velocity, $\overline{\rho}(z)$ is the density of the base-state environment, p' is the pressure perturbation, and B is the buoyancy. Furthermore, p' can be decomposed into dynamic pressure perturbation p'_d arising from variations in the velocity field and buoyancy pressure perturbation p'_b due to changes in density. The vertical momentum equation can then be written as

$$\frac{dw}{dt} = -\frac{1}{\overline{\rho}}\frac{\partial p'_d}{\partial z} + \left(-\frac{1}{\overline{\rho}}\frac{\partial p'_b}{\partial z} + B\right). \tag{3}$$

The first term on the right-hand side of Eq. (3) is dynamic VPPGF (DVPPGF). The two terms in the parentheses on the right-hand side are independent of the choice of the somewhat arbitrary base-state $\overline{\rho}(z)$ profile (Doswell and Markowski 2004) and are referred to as the effective buoyancy (EB) term with p'_b being the perturbation pressure induced by buoyancy.

Such a decomposition of vertical momentum is widely employed in studies of supercells (e.g., Davenport and Parker 2015; Warren et al. 2017; Huang and Xue 2025). The p'_b is calculated by solving the Poisson equation:

$$\nabla^2 p'_b = \frac{\partial \overline{\boldsymbol{\rho}} B}{\partial z}, \tag{4}$$

and p'_d is obtained by subtracting p'_b from total perturbation $\boldsymbol{p}'$ produced by the model, which represents the deviation of pressure from the base state (Markowski and Richardson 2010). The p'_d can be further divided into the parts due to the splat and spin terms within the p'_b diagnostic equation (Huang and Xue 2025):

$$p'_d = p'_{d_{\text{splat}}} + p'_{d_{\text{spin}}}. \tag{5}$$

The splat term is connected to flow convergence and deformation, which describe the extent to which a fluid element's

Brought to you by UNIVERSITY OF OKLAHOMA LIBRARY | Unauthenticated | Downloaded 10/27/26 06:31 PM UTC

TABLE 2. List of acronyms.

Acronym	Description
CTRL	A control supercell simulation without sea-breeze interference
CMBL	Cold marine boundary layer
DVPPGF	Dynamic vertical perturbation pressure gradient force term in the Lagrangian vertical momentum equation
EB	Effective buoyancy term in the Lagrangian vertical momentum equation
NDVPPGF	The DVPPGF induced by the spin term (fluid rotation)
TDVPPGF	The DVPPGF induced by the splat term (flow convergence and deformation)

shape changes under spatial velocity variations. The DVPPGF induced by this term is referred to as TDVPPGF. The spin term is related to fluid rotation, and the related DVPPGF is referred to as NDVPPGF. Table 2 summarizes the acronyms used in this paper. To isolate the effects of convergence/deformation and rotation induced by a sea-breeze front on supercell updrafts, $p'_{d_{\text{splat}}}$ and $p'_{d_{\text{spin}}}$ are obtained by solving Eqs. (6) and (7), respectively:

$$\nabla^2 p'_{d_{\text{splat}}} = -\overline{\rho} e_{ij}^2 = -\frac{1}{4}\overline{\rho}\sum_{i=1}^{3}\sum_{j=1}^{3}\left(\frac{\partial u_i}{\partial x_j}+\frac{\partial u_j}{\partial x_i}\right)^2, \tag{6}$$

$$\nabla^2 p'_{d_{\text{spin}}} = \frac{1}{2}\overline{\rho}|\boldsymbol{\omega}|^2, \tag{7}$$

where $\boldsymbol{\omega}$ is the vorticity vector. The Poisson equations to solve for p'_d and p'_b are available inside the CM1 model source code, using a horizontal Fourier transform combined with a vertical tridiagonal solver. The lateral boundary conditions are periodic. The bottom and top boundary conditions are Neumann type with zero vertical gradient for perturbation pressure. An offline version of the Poisson equation solver was used to solve Eqs. (6) and (7) for $p'_{d_{\text{splat}}}$ and $p'_{d_{\text{spin}}}$. In Huang and Xue (2025), the contributions of dynamic perturbation pressure associated with the splat and spin terms and the resulting vertical dynamic pressure gradient forces on tornado intensification and maintenance within a simulated supercell are analyzed in detail. In section 3d, we will perform diagnostic analyses of the perturbation pressure to investigate the dynamic effects on the supercell storm evolution.

3. Results

a. *Control supercell simulation*

The top row in Fig. 2 presents the development of the CTRL supercell over time. In CTRL, the warm bubble develops into an isolated convection cell and begins to split into right-moving and left-moving cells before $t = 60$ min. The right-moving cell evolves into a mature supercell by $t = 120$ min, while the left mover is much weaker. This study focuses solely on the development of the right-moving supercell, with the centroid of grid points where midlevel ($z \sim 6$ km) vertical velocity w exceeds 10 m s^{-1} used to track its center location.

b. *General characteristics of simulated supercells with sea-breeze interactions*

Rows 2–5 in Fig. 2 show the storm development in four coastal supercell simulations. In all coastal simulations, the CMBL air starts to influence storms by ~60 min and collides with the storm's cold pool by ~90 min (as indicated by the rightmost blue negative-buoyancy contour in the first two columns of rows 2–5 in Fig. 2). After $t = 90$ min, the reflectivity patterns in the $h = 500$ m CMBL simulations resemble those of CTRL, while their midlevel updraft areas tend to be slightly smaller than CTRL, particularly in CMBL500_5. However, storms in CMBL1500_3 and CMBL1500_5, which encounter stronger sea-breeze flows, exhibit noticeably larger midlevel updraft areas and higher radar reflectivity in the forward flank. Additionally, intensified low-level convergence within these supercells induces strong upward motion, accompanied by an expansion of the *V*-shaped notch in reflectivity.

The accumulated effects of the CMBL on supercells can be more directly observed from Fig. 3, which shows the accumulated surface rainfall and the tracks of the right-moving supercell center from different simulations. The stronger, deeper sea-breeze air in CMBL1500_3 and CMBL1500_5 reduces the forward movement speed of the supercell and increases its rightward deviation. During 60–140 min, all four coastal simulations produce greater rainfall than CTRL. After $t = 140$ min, the $h = 1500$ m experiments produce significantly more rainfall than CTRL, with precipitation becoming more intense as the absolute value of θ'_0 increases.

As mentioned earlier, the CMBL air not only brings strong eastward-moving winds but also induces a local temperature deficit. Figures 4a–c illustrate how variations in CMBL h and θ'_0 influence the inflow environments, as reflected by changes in vertical wind shear, storm-relative helicity (SRH), and CAPE. The inflow region is defined as the area located 30 km southeast of the maximum 2–5-km updraft helicity (indicating the center of rotating updraft), similar to the approach of Riggin et al. (2025). As in Lombardo and Kading 2018, the strength of sea-breeze flow is more sensitive to the CMBL h than to θ'_0. After $t = 60$ min, the inflow low-level shear of all coastal simulations begins to increase to approximately 8 m s^{-1}, while in the CTRL simulation, it remains nearly constant at around 5.5 m s^{-1} (Fig. 4a). As time progresses, the $h = 1500$ m runs sustain a significantly higher shear, whereas the wind shear associated with the $h = 500$ m runs decreases and eventually becomes only slightly larger than that of CTRL. It is noteworthy that the temporal variation of 0–1-km inflow SRH across different simulations differs from that of the 0–1-km shear (Fig. 4b). A noticeable increase in 0–1-km SRH is not observed until the later stage of the sea-breeze-influenced supercells, most evident in CMBL1500_5 (~121 m^2 s^{-2}), when the sea-breeze front passes completely beneath the updraft and the inflow region

Brought to you by UNIVERSITY OF OKLAHOMA LIBRARY | Unauthenticated | Downloaded 10/27/26 06:31 PM UTC

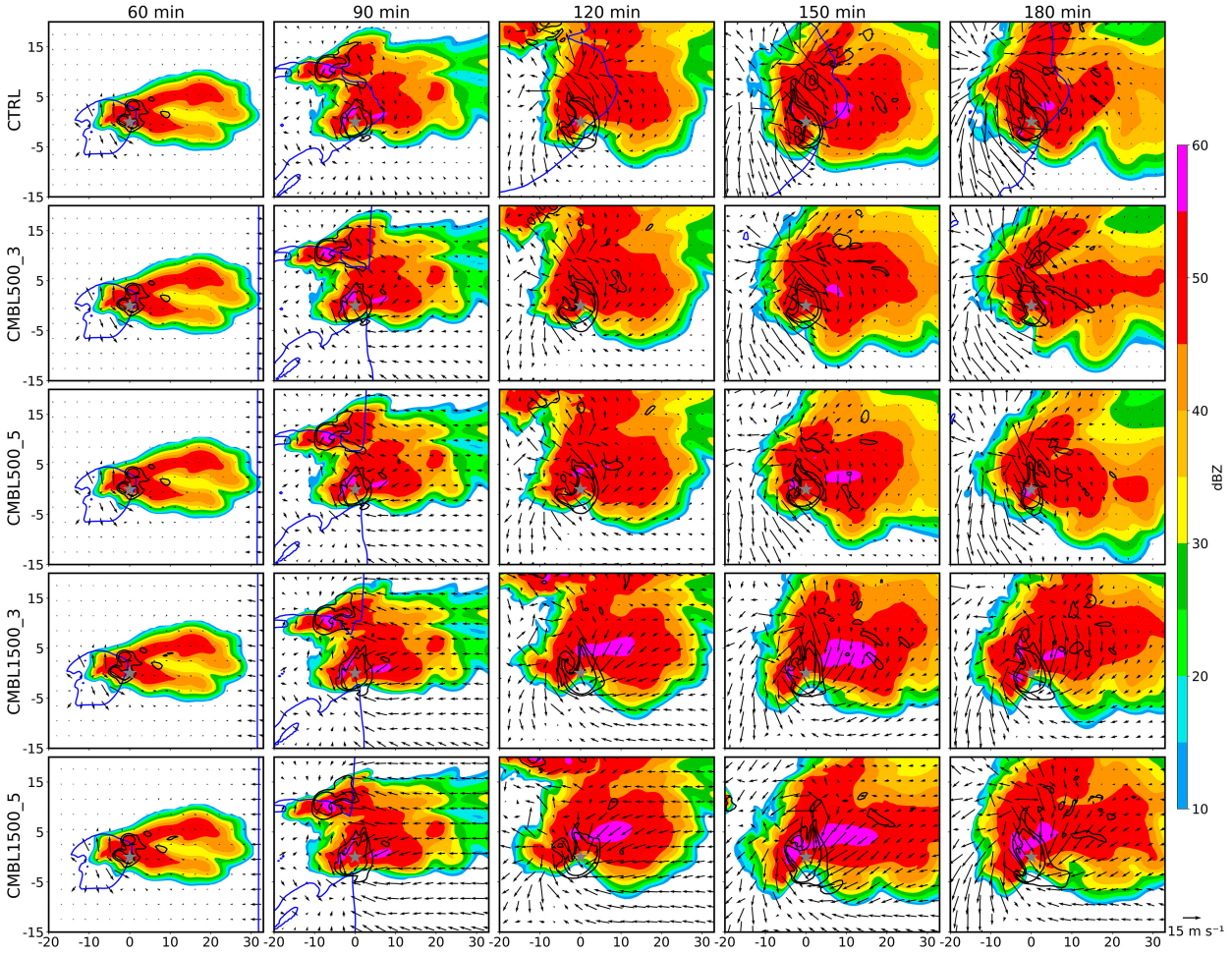


FIG. 2. Evolution of the supercell for (first row) CTRL, (second row) CMBL500_3, (third row) CMBL500_5, (fourth row) CMBL1500_3, and (fifth row) CMBL1500_5. Shaded contours (radar reflectivity Z), ground-relative wind vectors, and blue contour lines (-0.05 m s^{-2} buoyancy) depict fields at the model's lowest model level (50 m) above ground, and the reference vector is located at the bottom-right corner. Black contour lines represent vertical velocities of 5 and 15 m s^{-1} at $z = 6$ km. The gray star denotes the center of right-moving storm. The x–y coordinates are shown relative to the storm center.

becomes influenced by the persistent, strong postfrontal flows. In addition, the $\theta_0' = -5$ K runs induce reductions in surface-based CAPE (SBCAPE) of approximately 1000 J kg^{-1}, while the $\theta_0' = -3$ K runs have smaller decreases of about 400 J kg^{-1} (Fig. 4c).

Beyond parameters of the inflow environment, several storm-scale parameters are used to quantify the influence of the sea-breeze flows on the supercells (Figs. 4d–g). The favorable low-level inflow SRH conditions associated with the deep CMBL ($h = 1500$ m) cases lead to significantly enhanced 2–5-km updraft helicity (~60 m^2 s^{-2}) during the later stage (Fig. 4d), whereas no obvious enhancement of 6-km updraft vertical velocity is observed throughout the entire stage (Fig. 4e). After the intrusion of CMBL air into the updraft at 90 min, the 6-km maximum w in all sea-breeze simulations becomes smaller than that of CTRL (CMBL cases ~42 m s^{-1}, CTRL ~45 m s^{-1} at 105 min; Fig. 4e), apparently due to the reduced CAPE. After 120 min, the 6-km maximum w in all sea-breeze cases except CMBL1500_5 recovers to nearly match that in CTRL. The reduced w in CMBL1500_5 is likely due to the greatest reduction in CAPE and hence updraft buoyancy. Corresponding to the weakest updraft, the intensity of midlevel mesocyclone (as indicated by the maximum vertical vorticity at the 6-km level) in CMBL1500_5 is also the weakest (associated with the weakest vertical stretching; Fig. 4f). Although the midlevel mesocyclone in CMBL1500_5 is weaker, its total condensate mass (~9×10^9 kg) is actually substantially higher than that of CTRL, and CMBL1500_3 has the second largest condensate mass (~6×10^9 kg; Fig. 4g), matching the precipitation amounts shown in Fig. 3. The majority of updraft characteristics in CMBL500_3 and CMBL500_5 resemble those in CTRL.

The significantly greater accumulated surface rainfall (Fig. 3), along with the increased total condensate mass (Fig. 4g) in the $h = 1500$ m simulations, may be related to the overall larger updrafts. A more detailed analysis of vertical velocity, vertical vorticity, updraft area, and condensate mass at different heights

Brought to you by UNIVERSITY OF OKLAHOMA LIBRARY | Unauthenticated | Downloaded 10/27/26 06:31 PM UTC

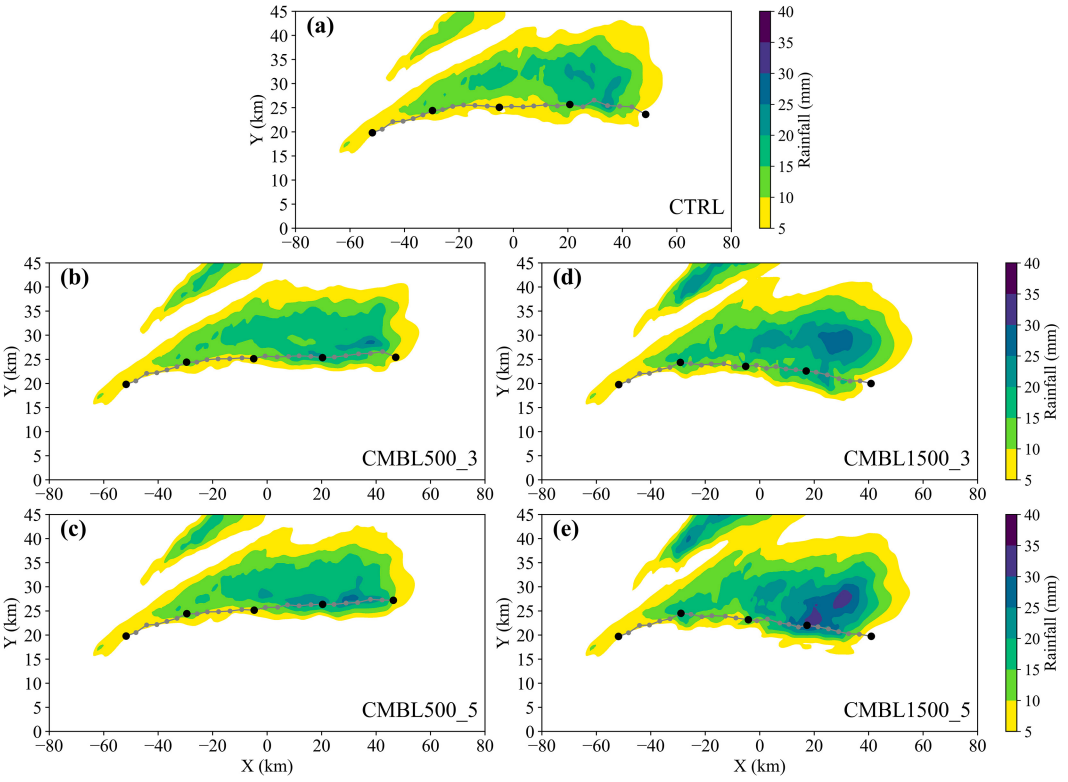


FIG. 3. Accumulated surface rainfall (mm) for (a) CTRL, (b) CMBL500_3, (c) CMBL500_5, (d) CMBL1500_3, and (e) CMBL1500_5. The trajectory of the right-moving supercell center from 60 to 180 min is marked by dots in each panel. Black and gray dots indicate times at 30- and 5-min intervals, respectively. The center of the model domain is located at ($x = 0$) km.

within regions of strong updrafts ($w > 10$ m s^{-1}) averaged from $t = 90$ to 180 min is presented in Fig. 5. Below the level of 4 km, all simulations exhibit similar vertical velocities (~20 m s^{-1} at 3 km), and the maximum vertical vorticities in CMBL1500_3 (~0.017 s^{-1} at 3 km) and CMBL1500_5 (~0.019 s^{-1} at 3 km) are progressively stronger than in CTRL (~0.015 s^{-1} at 3 km; Figs. 5a,b). Above 6 km, however, both vertical velocity and vorticity in $h = 1500$ m simulations (vertical velocity ~47 m s^{-1} and vorticity ~0.038 s^{-1} in CMBL1500_3; ~49 m s^{-1} and ~0.033 s^{-1} in CMBL1500_5 at 8 km) become noticeably weaker than those in CTRL (~51 m s^{-1} and ~0.044 s^{-1} at 8 km). In contrast, the $h = 500$ m simulations (shallower sea-breeze flows) show vertical velocity and vorticity values comparable to those in CTRL. Consistently forced by strong opposing winds at the outflow levels, the updraft areas in the $h = 1500$ m cases are significantly larger than that in CTRL at all altitudes where updrafts are present, with CMBL1500_5 exhibiting the largest updraft area (e.g., ~62 m^2 in CMBL1500_5, while ~43 m^2 in CTRL at 6 km; Fig. 5c). During the later stage, the low-level updraft exhibits a more upright orientation in the $h = 1500$ m runs than that in CTRL (not shown). An updraft that is more upright and spans a larger area can better resist entrainment and facilitate storm development (McCaul and Cohen 2002; Weisman et al. 1988), potentially offsetting, at least to some extent, the negative effects of cold and stable sea-breeze air. Figure 5d further shows that the condensate mass is closely related to the updraft area, with the $h = 1500$ m runs exhibiting the largest values (e.g., with maximum values of ~7×10^7 kg in $h = 1500$ m runs and ~5×10^7 kg in CTRL). In addition, the vertical distributions of updraft area and condensate mass in the $h = 500$ m runs are mostly similar to those in CTRL (Figs. 5c,d).

c. *CMBL effects on inflow and updraft characteristics*

We first examine the effects of sea-breeze flows on the low-level wind profiles. The inflow region is identified using the same method described in section 3b. After the sea-breeze flows start to collide with the cold pool (at ~90 min), their influence on the inflow can be divided into two stages: the early stage (90–140 min) and the later stage (140–180 min). In the early stage, the sea-breeze flows cause the low-level [~ 500 m above ground level (AGL)] inflow hodograph to bend westward (e.g., the first two rows of the rightmost column of Fig. 6 for CMBL1500_5). The orientation of low-level (approximately below 500 m AGL) horizontal vorticity in the layer influenced by the strong sea-breeze flow (in $h = 1500$ m cases) is more crosswise, which is most evident in the CMBL1500_5 simulation (as indicated by the blue and purple arrows showing horizontal vorticity and storm-relative velocity at 500 m AGL in Fig. 6). However, above 500 m AGL, the horizontal vorticity exhibits a smaller crosswise component, and the storm-relative velocity over 0–1 km is larger (not shown).

Brought to you by UNIVERSITY OF OKLAHOMA LIBRARY | Unauthenticated | Downloaded 10/27/26 06:31 PM UTC

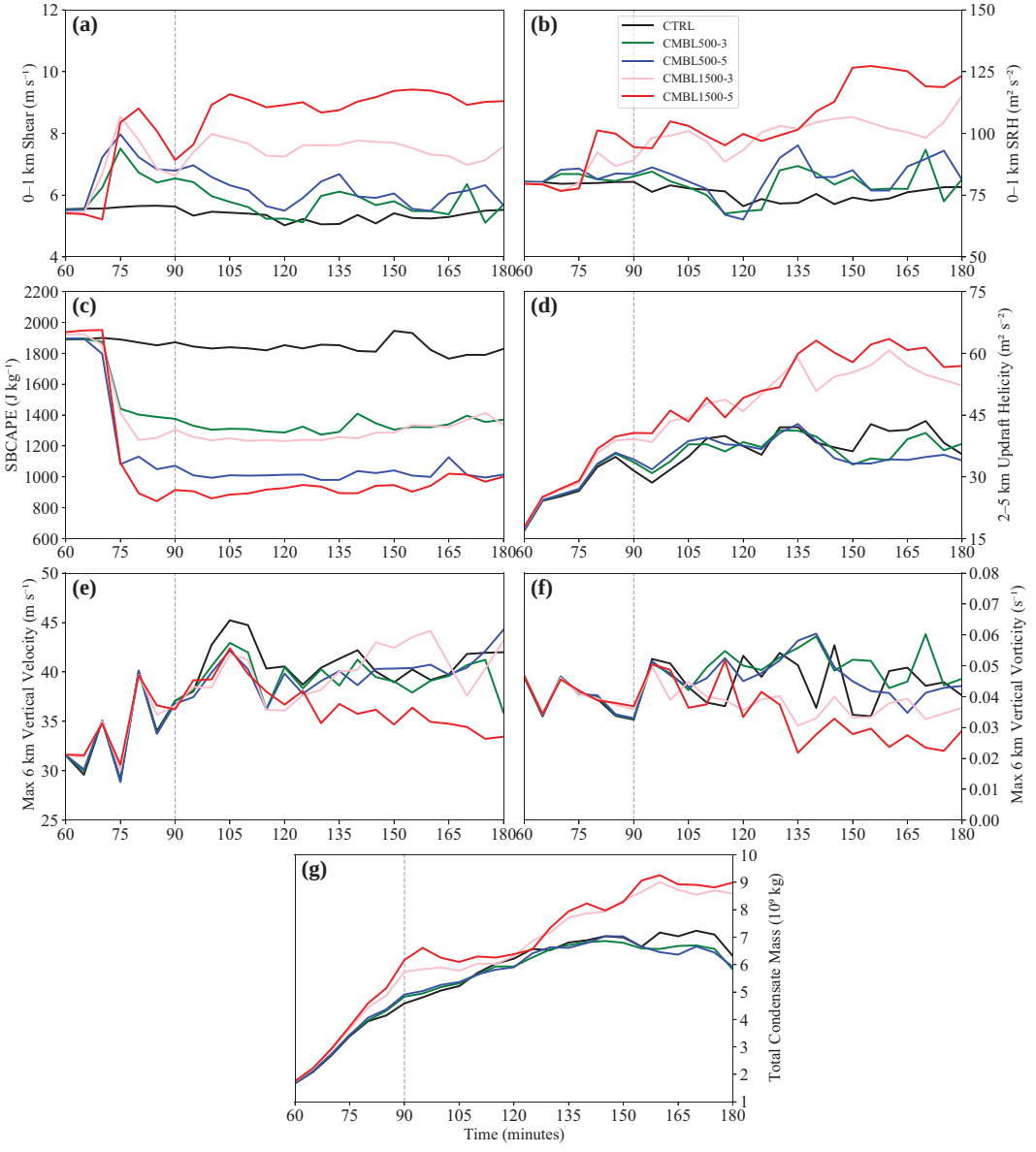


FIG. 4. Evolution from 60 to 180 min of (a) 0–1-km shear, (b) 0–1-km SRH, and (c) SBCAPE in the inflow environment, and (d) mean 2–5-km updraft helicity, (e) maximum vertical velocity at 6 km, (f) maximum vertical vorticity at 6 km, and (g) total condensate mass, all computed within a 20 km × 20 km area centered on the storm location for five simulations. The black line denotes the CTRL. The red, pink, blue, and light blue lines represent the CMBL1500_5, CMBL1500_3, CMBL500_5, and CMBL500_3, respectively. The gray line in (a) marks the time when the sea-breeze air collides with the updraft.

Consequently, the total 0–1-km SRH in the $h = 1500$ m cases is slightly higher than in CTRL (e.g., 0–1-km SRH in CMBL1500_5 is ~89 m^2 s^{-2}, compared to ~75 m^2 s^{-2} in CTRL; Fig. 4b). During the early stage, the updraft may ingest less streamwise vorticity in the $h = 1500$ m runs, particularly in CMBL1500_5, leading to weaker mesocyclones. In addition, although the 0–1-km SRH (Fig. 4b) is larger in CMBL1500_5 than that in CTRL, this increase in inflow SRH is still insufficient for the updraft to overcome the negative thermal effects of the cold CMBL air. These factors result in weaker updrafts (as suggested by the condensate mixing ratio) in CMBL1500_5 compared to CTRL (Figs. 7a,b,e,f).

After the sea-breeze front totally passes underneath the main updraft during the later stage, the westward bending of the low-level hodograph is decreased (the third and fourth rows in Fig. 6). Hence, the horizontal vorticity becomes more aligned with the storm-relative flow direction again, although it remains more northward compared to CTRL. The higher low-level inflow SRH in the sea-breeze simulations is not due to a better alignment between low-level horizontal vorticity

Brought to you by UNIVERSITY OF OKLAHOMA LIBRARY | Unauthenticated | Downloaded 10/27/26 06:31 PM UTC

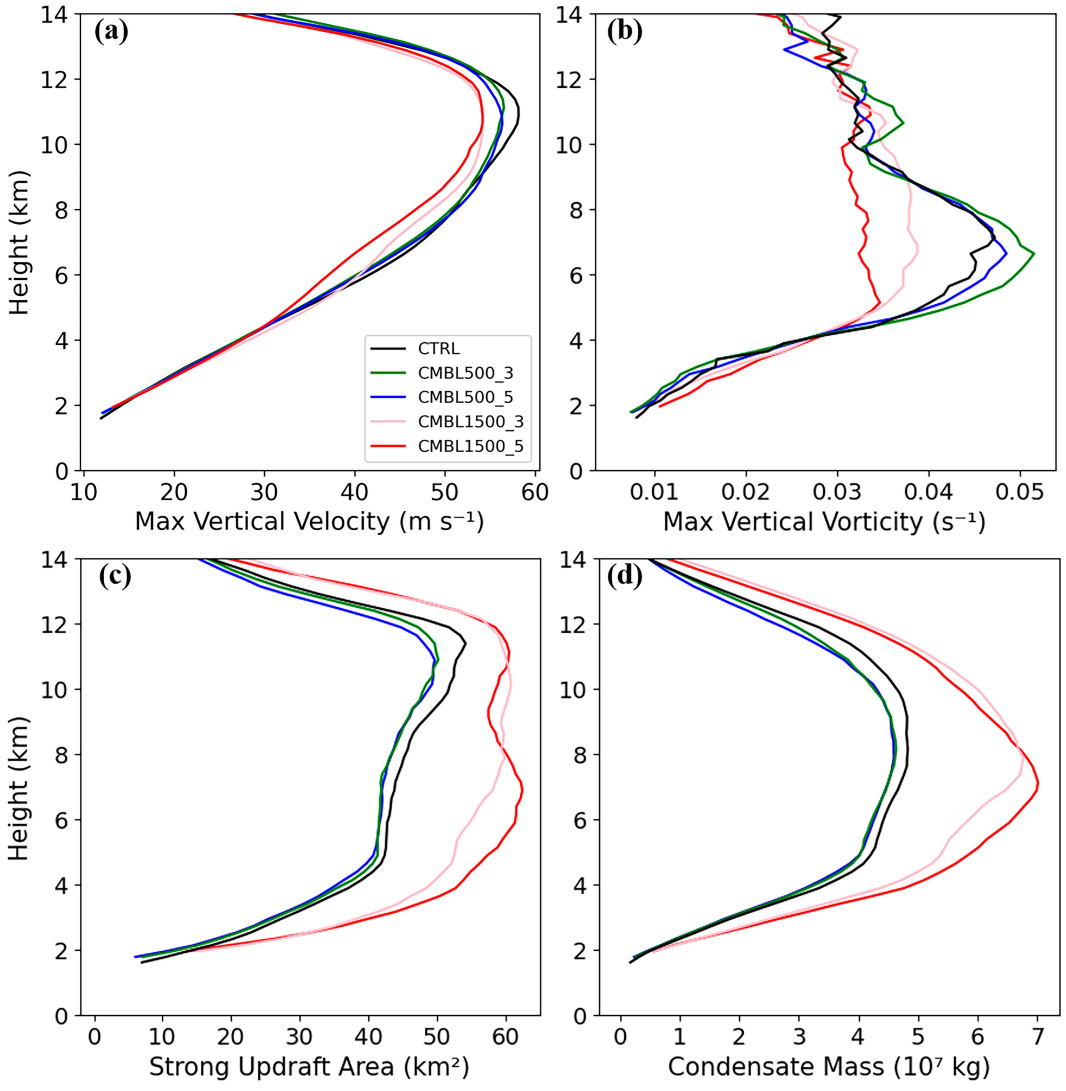


FIG. 5. Time-averaged (90–180 min) vertical profiles of (a) max vertical velocity, (b) max vertical vorticity, (c) strong updraft area, and (d) condensate mass of updraft ($w > 10$ m s^{-1}). All computed within a 20 km × 20 km area centered on the storm location for five simulations. The black line denotes the CTRL. The red, pink, blue, and light blue lines represent the CMBL1500_5, CMBL1500_3, CMBL500_5, and CMBL500_3, respectively.

and storm-relative wind but rather to larger values of horizontal vorticity and storm-relative velocity. The intrusion of low-level easterly sea-breeze flows leads to enhanced westerly shear with height and a northward veering of low-level horizontal vorticity, which deviates from the streamwise direction of the storm-relative velocity. Increased 0–1-km SRH should help increase the updraft rotation and promote stronger updrafts through the dynamic effect of decreased pressure at the mesocyclone center. With an increase in low-level vorticity and flow speed, the inflow 0–1-km SRH increases significantly in $h = 1500$ m runs during this later stage (e.g., 0–1-km SRH in CMBL1500_5 is ~121 m^2 s^{-2}, while that in CTRL is ~75 m^2 s^{-2}; Fig. 4b). The substantially larger low-level inflow SRH during the later stage contributes to stronger updrafts in $h = 1500$ m runs (Figs. 7c,d,g,h) and heavier prediction (Fig. 3e) than those in CTRL.

d. *CMBL effects on dynamic pressure gradient force and buoyancy*

Changes in low-level flows and vertical wind shear can lead to DVPPGF that directly affect updraft intensity, while changes in the temperature of low-level air can give rise to variations in buoyant acceleration of updraft (Davenport and Parker 2015). To isolate the effects of the flow field and the temperature of sea-breeze air on the updraft, the right-hand-side force of the vertical momentum equation is decomposed into DVPPGF and EB according to Eq. (3). The DVPPGF and EB averaged over 90–180 min of simulations and in the updraft region where $w > 10$ m s^{-1} (within a 20 km × 20 km

Brought to you by UNIVERSITY OF OKLAHOMA LIBRARY | Unauthenticated | Downloaded 10/27/26 06:31 PM UTC

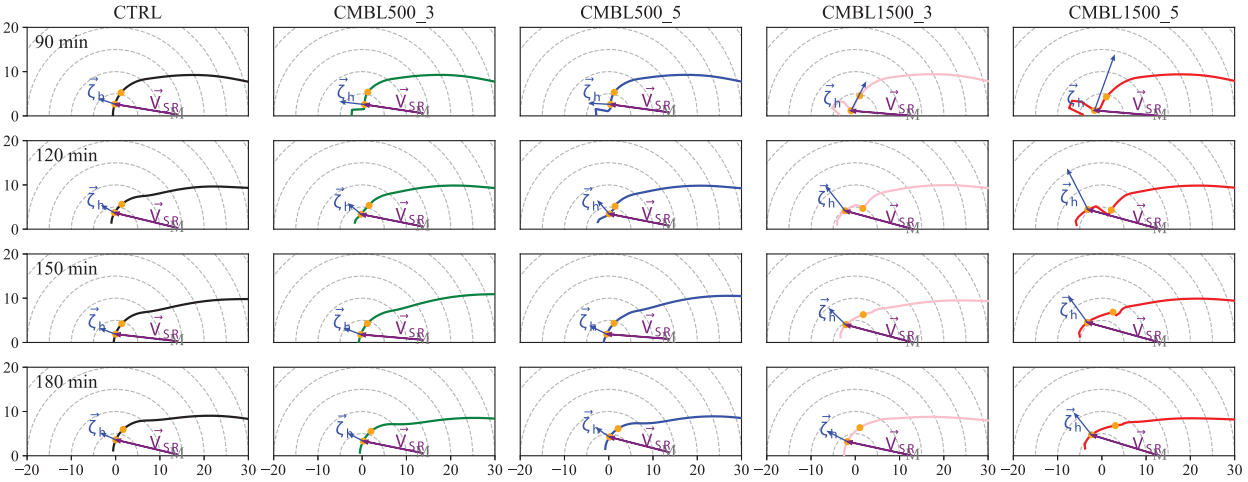


FIG. 6. Evolution of the inflow region hodograph during (first row),(second row) the early stage and (third row),(fourth row) the later stage for (first column) CTRL, (second column) CMBL500_3, (third column) CMBL500_5, (fourth column) CMBL1500_3, and (fifth column) CMBL1500_5. The dashed circles represent isotachs at 5 m s^{-1} intervals. The yellow dots denote 500 m and 1 km in heights. The blue and purple arrows are horizontal vorticity $\boldsymbol{\zeta}_h$ and storm-relative velocity $\mathbf{V}_{SR}$ at 500 m in height, respectively. The letter "M" marks the storm motion velocity.

area centered on the simulated storm) are shown in Fig. 8. They are directed upward below ~7 and ~9.5 km AGL, respectively, and the lower-level (up to ~5 km AGL) values of DVPPGF are larger than EB in all simulations (Fig. 8). The sea-breeze flows clearly enhance the low-level DVPPGF within the supercell updraft, with the h = 1500 m runs exhibiting the strongest positive effects (e.g., ~0.06 m s^{-2} in h = 1500 m runs, while ~0.05 m s^{-2} in CTRL at 3 km; Fig. 8a). Conversely, EB in the h = 1500 m runs is consistently lower than those in CTRL from low levels to approximately 9 km due to decreased CAPE (e.g., with maximum values of ~0.04 in CMBL1500_3, ~0.03 in CMBL1500_5, and ~0.06 in CTRL; Fig. 8b). Due to persistently lower EB in the h = 1500 m cases, the midlevel updraft weakens (cf. Fig. 5a), which, in turn, leads to reduced DVPPGF at the mid–higher levels. However, at low levels, the enhanced upward DVPPGF associated with the sea-breeze

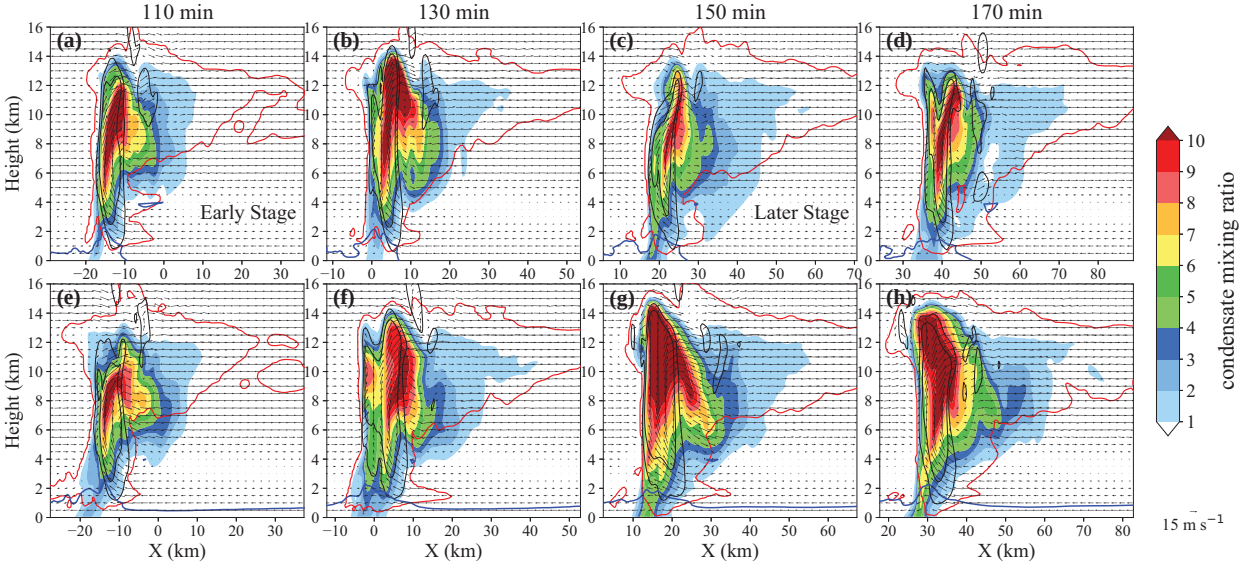


FIG. 7. Vertical cross sections for (top) CTRL and (bottom) CMBL1500_5 during the (first column),(second column) early stage (90–140 min) and (third column),(fourth column) the later stage (140–180 min) of supercell evolution and sea-breeze front interaction. The cloud boundary ($q_c + q_i$ = 0.01 g kg^{-1}) is indicated by the red lines. Contours of 5 and 15 m s^{-1} vertical velocity (black lines), −0.05 m s^{-2} buoyancy (blue lines), and total condensate mixing ratio (filled contours). Vectors are storm-relative wind. The reference vector is located at the bottom-right corner. Cross sections are taken from west to east through the storm center (based on ~6-km vertical velocity) with values averaged over a width of 5 km.

Brought to you by UNIVERSITY OF OKLAHOMA LIBRARY | Unauthenticated | Downloaded 10/27/26 06:31 PM UTC

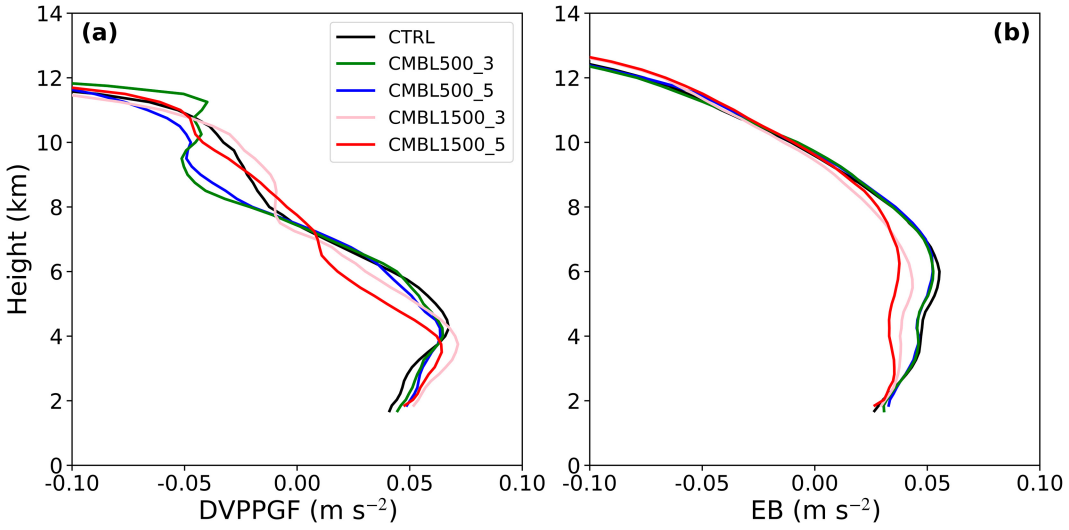


FIG. 8. Time-averaged (90–180 min) vertical profiles of mean values of (a) DVPPGF and (b) EB in the vertical momentum equation for updraft ($w > 10$ m s^{-1}). All computed within a 20 km × 20 km area centered on the storm location for five simulations. The black line denotes the CTRL. The red, pink, blue, and light blue lines represent the CMBL1500_5, CMBL1500_3, CMBL500_5, and CMBL500_3, respectively.

flows compensates for the reduced upward EB caused by the cooler inflow air, allowing the vertical velocity in the $h = 1500$ m runs to approach that of CTRL (Fig. 5a). The cooler air associated with the shallower CMBL ($h = 500$ m) has minimal impact on the buoyancy of the updrafts, as the EB is only slightly lower at certain altitudes than that in CTRL (Fig. 8b).

The sea-breeze flows can enhance the low-level DVPPGF for updrafts, but exactly how this is achieved is not clear, and the effects may be different at different stages of the front–storm interaction. Apart from the effects of rotation on DVPPGF through the spin term in Eq. (6), DVPPGF can also be induced by divergence and deformational flows, as described by the splat term in Eq. (6). To see what relative roles each type of flow plays, we decompose DVPPGF into TDVPPGF and NDVPPGF and show them in Fig. 9 as vertical profiles, again averaged over the updraft regions as before, but over time periods of 90–140 min (the early stage) and 140–180 min (the later stage). Overall, TDVPPGF is generally negative (except for the 1500-m CMBL cases in the early stage at the gust levels; an example is shown for CMBL1500_5 in Fig. 10), while NDVPPGF is positive within the updraft region for all simulations (Figs. 9b,e). The positive NDVPPGF is due to the updraft rotation or mesocyclone that creates negative perturbation pressure at the mid–upper levels. The generally positive total DVPPGF below the 4-km level (Fig. 9) is a result of the larger magnitude of positive NDVPPGF than that of negative TDVPPGF.

During the early stage, a strong westward-moving sea-breeze front collides with the outflow of the eastward-moving supercell. The convergence-/deformation-related negative TDVPPGF becomes smaller in magnitude (Fig. 9a) and turns positive near the gust-front level, particularly for CMBL1500_5 (Fig. 10). As discussed above, the updraft in CMBL1500_5 is weaker than that in CTRL (Fig. 8) during the early stage. This weakening may be related to the ingestion of less streamwise vorticity by the inflow and the insufficient compensation of the negative thermal effect of the cold CMBL air by the slightly larger 0–1-km SRH compared to CTRL. CMBL1500_3 is similar, but the updraft in CMBL1500-3 is not as weak as that in CMBL1500-5 with the less cold sea-breeze air. Therefore, the NDVPPGF (which is related to updraft rotation) in $h = 1500$ m cases (especially CMBL1500_5) is smaller than in other cases during the early stage (Fig. 9b). Despite that, DVPPGF, the sum of TDVPPGF and NDVPPGF, is actually larger in $h = 1500$ m cases (Fig. 9c).

After the sea-breeze front passes through underneath the updraft, the steady sea-breeze flow behind the front provides larger inflow SRH, especially for the $h = 1500$ m cases, as discussed earlier (Fig. 4b). The 2–5-km updraft helicity measuring the intensity of rotating low–midlevel updraft is significantly increased (e.g., 2–5-km updraft helicity in CMBL1500_5 is ~60 m^2 s^{-2}, while that in CTRL is only ~39 m^2 s^{-2}; Fig. 4d), and updraft becomes stronger (Figs. 7g,h) during the later stage. Therefore, the upward NDVPPGF becomes larger than CTRL in the $h = 1500$ m cases during this period, leading to larger positive low-level DVPPGF (Fig. 9f). NDVPPGF in the $h = 500$ m cases is slightly larger than in CTRL during both the early and later stages, which may be related to the higher low-level SRH environment compared to CTRL (Fig. 4b) and the smaller negative thermal effect compared to the $h = 1500$ m cases (Fig. 8b). The dynamic and thermodynamic characteristics in CMBL500_5 lead to a higher mean updraft vertical velocity (~2–4 km) compared to CMBL1500_5 (not shown), which may, in turn, cause the mean NDVPPGF in CMBL500_5 to be slightly larger than in CMBL1500_5 during the later stage (Fig. 9e). However, TDVPPGF in $h = 500$ m cases is generally smaller (more negative) in both stages (Figs. 9a,d), leading to lower low-level DVPPGF compared to the $h = 1500$ m cases (Figs. 9c,f). In addition, the low-level DVPPGF in the $h = 1500$ m

Brought to you by UNIVERSITY OF OKLAHOMA LIBRARY | Unauthenticated | Downloaded 10/27/26 06:31 PM UTC

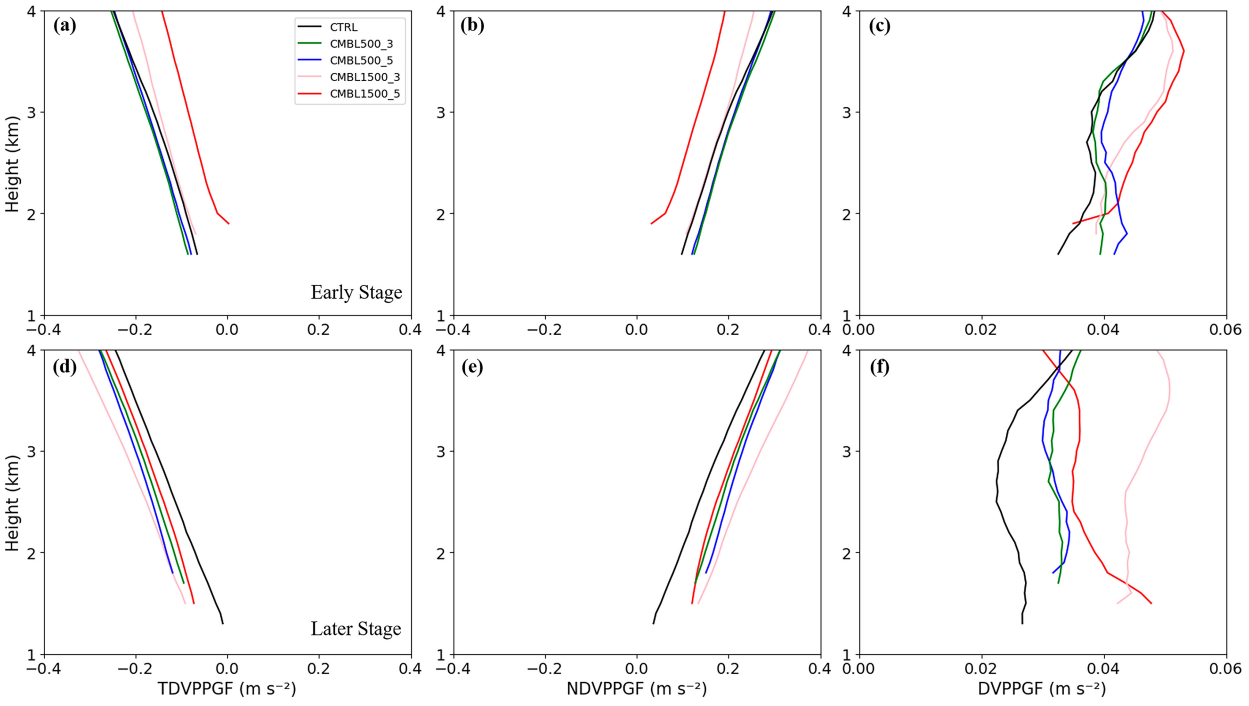


FIG. 9. Time-averaged vertical profiles of the mean TDVPPGF, NDVPPGF, and DVPPGF for updraft regions with $w > 10$ m s^{-1}, during (a)–(c) the early stage (90–140 min) and (d)–(f) the later stage (140–180 min). All profiles are computed within a 20 km × 20 km area centered on the storm location for five simulations. The black line denotes CTRL, while the red, pink, blue, and light blue lines represent the CMBL1500_5, CMBL1500_3, CMBL500_5, and CMBL500_3 experiments, respectively.

cases is larger during the later stage than during the early stage (Figs. 9c,f). In conclusion, at the initial stage of the collision between the sea-breeze front and the supercell outflow in the deep and cold CMBL case (particularly in CMBL1500_5), the splat term associated with flow convergence and deformation enhances the total DVPPGF in the low-level updraft. At the later stage after the collision, the larger (cf. CTRL) positive DVPPGF due to the spin term related to the enhanced low-level inflow SRH and updraft rotation becomes the main factor enhancing the total DVPPGF of supercell updraft. This is true for all CMBL cases with different initial depth and coldness.

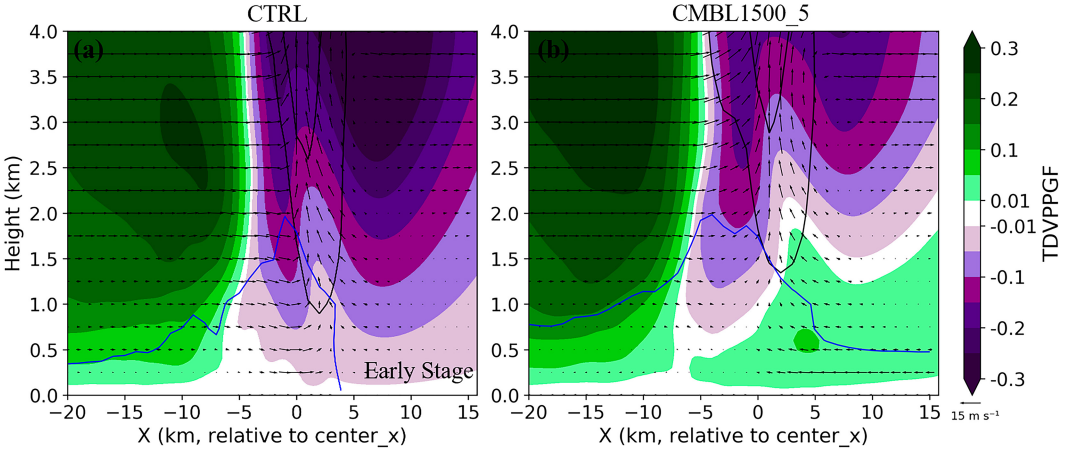


FIG. 10. Time-averaged vertical profiles for (a) CTRL and (b) CMBL1500_5 during the early stage (90–140 min). Shown are contours of 5 and 15 m s^{-1} vertical velocity (black lines), −0.05 m s^{-2} buoyancy (blue lines), and TDVPPGF (filled contours). Vectors are ground-relative wind. The reference vector is located at the bottom-right corner. Cross sections are taken from west to east through the storm center with values averaged over a width of 5 km.

Brought to you by UNIVERSITY OF OKLAHOMA LIBRARY | Unauthenticated | Downloaded 10/27/26 06:31 PM UTC

e. Parcel trajectory analyses

Some studies have suggested that stable boundary layer intrusion may lead to elevated updraft air sources in some storms (Davenport and Parker 2015), whereas in others, updraft parcels remain surface based (Parker 2008; Billings and Parker 2012). These differences may be related to variations in wind field configurations and storm intensity. The updraft parcel source region under the influence of CMBL to squall line has been studied by Lombardo and Kading (2018). Lombardo and Kading (2018) revealed that all parcels within and above $\theta_0' = -2$ K CMBL with various heights of parcels (250, 500, and 1000 m) rise into the storm. Storms moving over a $\theta_0' = -5$ K CMBL are partially elevated with their inflow source becoming increasingly elevated as the depth of CMBL increases. Within the coldest CMBL ($\theta_0' = -8$ K), only a negligible portion of air from the 500-m-deep layer ascends above 3 km. However, the study by Lombardo and Kading (2018) does not focus on the continuous evolution of storm parcels but rather on updraft parcel source at specific discrete times. To examine the influence of CMBL on the evolution of updraft parcels for supercells, forward trajectory analysis is performed for all simulations by releasing parcels at 60 min within a domain spanning $x = -50$ to 50 km, $y = -50$ to 50 km, and $z = 0$ to 4 km, with horizontal spacings of 500 m and vertical spacings of 100 m. This release region includes parcels ahead of sea-breeze front and a majority of parcels in the postfrontal region. In CM1, the air parcel trajectories can be integrated forward in time as the model runs.

Figure 12 shows vertical cross sections of cloud outlines, updrafts, and the number of air parcels at 60 or 120 min that end up within the midlevel (~6 km) updraft at 120 or 180 min, as described in the caption. Figure 12a shows that the parcels ending up within the midlevel updraft in CTRL at 120 min are located upstream of the gust front within a layer more than 2.5 km deep and that the lower the parcels are, the farther they are from the gust front, indicating that the lower-level air feeds the updraft at a faster rate. The parcels ending up within the midlevel updraft at 180 min are located, not surprisingly, further upstream at 60 min, and the vertical distribution of the parcels is similar (Fig. 11b). By 120 min, these parcels have all moved to within 50 km from the gust front and with the near-surface ones clearly moving much faster.

In CTRL (Figs. 11a–c), the supercell updraft is predominantly surface based, whereas in the CMBL simulations (Figs. 11d–o), the elevated portion is more pronounced when encountering cooler air. In addition, notable variations are observed in the heights of parcels entering the midlevel updraft during different storm stages for the 1500-m CMBL.

In the cases with CMBL, a sea-breeze front with cold air behind different depths progresses toward the storm gust front, and the two fronts have merged by 120 min (Figs. 11d–o). In the cases of $h = 500$ m initial CMBL (Figs. 11d–i), almost all air parcels entering the midlevel updrafts at 120 or 180 min originate from above the pool of sea-breeze air. The distributions of the originating air parcels are otherwise similar to those of the CTRL case. This indicates that for the cases of relatively shallow sea-breeze flow, it is mostly the air above the cold sea-breeze flow that feeds the supercell storm.

In the cases of $h = 1500$ m initial CMBL (Figs. 11j–o), the origins of air parcels are quite different from the $h = 500$ m cases. For air parcels entering the midlevel updraft at 120 min, they are all located above the sea-breeze front surface (Figs. 11j,m), but for air parcels that arrive at the midlevel updraft at 180 min, a significant portion of the parcels are located below the sea-breeze frontal surface at 60 min (Figs. 11k,n), and these parcels progress toward the storm gust front within the sea-breeze flow through 120 min when the two fronts have merged (Figs. 11l,o). In CMBL1500_5, where the near-surface sea-breeze air is colder, there does exist a shallow surface layer where cold-air parcels cannot be ingested into the storm updraft (Figs. 11n,o). Still, the results indicate that after the two fronts merge, the storm is capable of ingesting colder CMBL air when the sea-breeze flow is sufficiently deep. Davenport and Parker (2015) found that as the background environment cooled, and helicity and deep-layer bulk shear decreased, the mean source region for updraft parcels became elevated, and fewer and drier parcels were ingested by supercells over time. In contrast, our 1500-m CMBL simulations show that under favorable dynamic conditions, the supercell updraft can ingest more near-surface parcels when surrounded by cool air. However, the ingestion of CMBL air into the storm would diminish deep convective latent heating, leading to reduced storm intensity and potentially storm decay (Alfaro 2017).

The cold pool of convective storms is known to play a significant role in convective organization through the gust front and baroclinic vorticity it generates (Rotunno et al. 1988; Markowski et al. 2008). The difference in ingested parcel heights over time in the 1500-m CMBL simulations could be linked to the cold-pool evolution in the supercell. In the CTRL simulation, no cold air originates from the CMBL, and the supercell cold pool gradually spreads in all directions, increasing in spatial coverage and intensity over time (Figs. 12a–d). As time passes, the minimum perturbation temperature is less than −6 K, and the gust-front temperature gradient is sharp, and gust front provides strong lifting to the inflow air to feed the updraft.

In the cases with a CMBL, the sea-breeze front first collides with the storm cold pool before 90 min (Figs. 12a,e,i,m,q) and becomes mostly merged with the cold pool by 120 min. In the cases of $h = 500$ m initial CMBL depth, the sea-breeze flows are rather shallow (Figs. 11d–i and 12e–l), the main effect of the sea-breeze flow is to displace the air parcels feeding the updraft by a couple of hundreds of meters above ground (cf. Fig. 11). The general flow and cold-pool patterns at the surface in $h = 500$ m runs are not too different from those of CTRL, and the differences in precipitation and updraft intensities are not very different either, as discussed earlier (Figs. 3 and 5). During the early stage, the cold pool does not exhibit a markedly greater strength than the 1500-m CMBL (Figs. 12m–t). The weak temperature gradient at the cold pool's leading edge leads to insufficient gust-front lifting, preventing colder CMBL parcels from being elevated into the updraft. After 120 min into the mature stage, increased precipitation results in a noticeably colder cold pool relative to the CMBL air (exceeding 2 K), enhancing the lifting capability of

Brought to you by UNIVERSITY OF OKLAHOMA LIBRARY | Unauthenticated | Downloaded 10/27/26 06:31 PM UTC

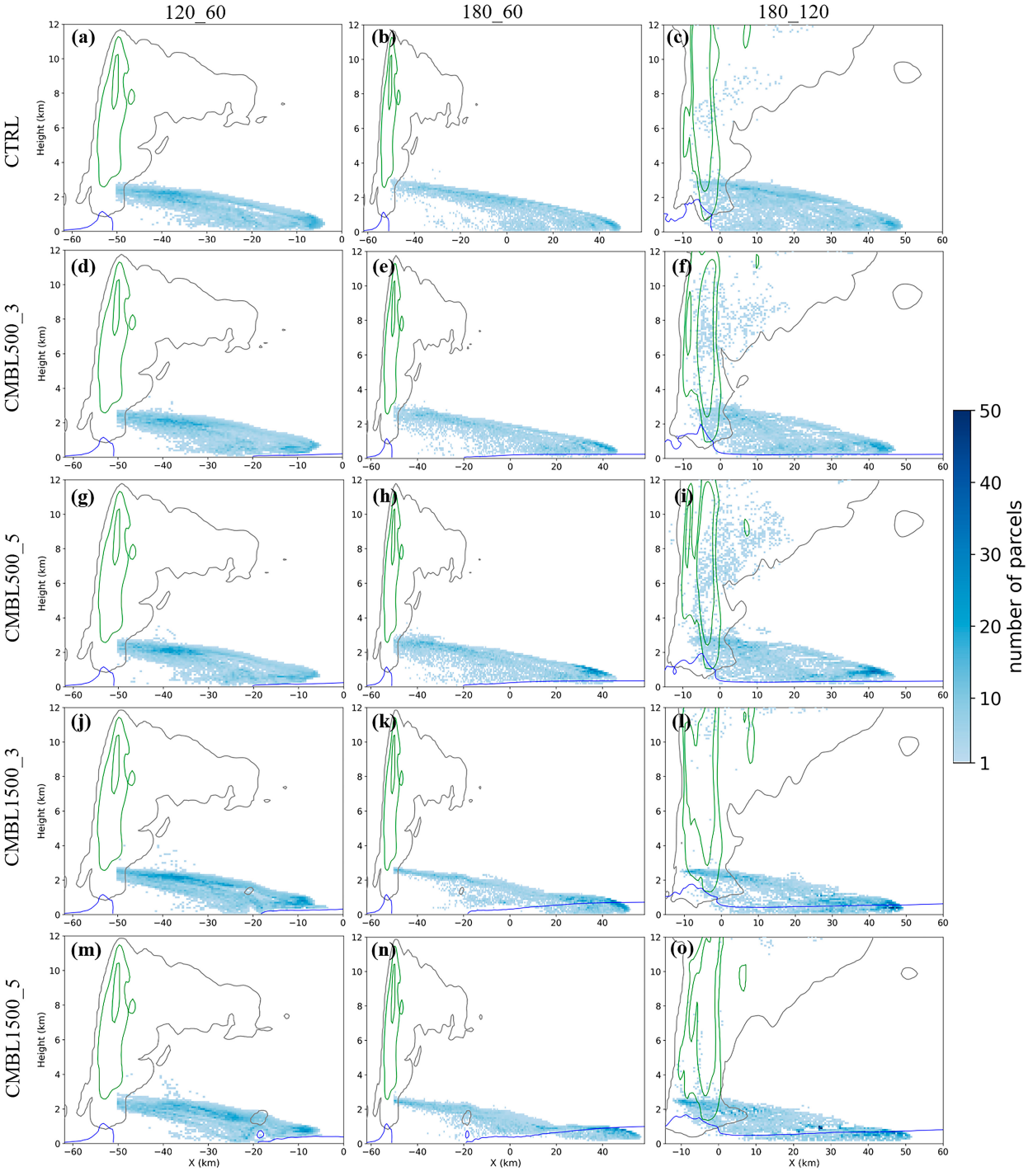


FIG. 11. Vertical cross sections for (first row) CTRL, (second row) CMBL500_3, (third row) CMBL500_5, (fourth row) CMBL1500_3, and (fifth row) CMBL1500_5. The cloud boundary ($q_c + q_i = 0.01$ g kg^{-1}) is indicated by the gray lines. Green contours indicate vertical velocity (5 and 15 m s^{-1}), blue contours indicate buoyancy (-0.05 m s^{-2}), and filled contours indicate the number of air parcels at the corresponding locations. The panels show the parcel distributions and associated fields at 60 min (left and middle) and 120 min (right). The selected parcels subsequently reside within the midlevel (~6 km) updraft at 120 min (left) and 180 min (middle and right). Cross sections are taken from west to east through the storm center with values averaged over a width of 5 km.

Brought to you by UNIVERSITY OF OKLAHOMA LIBRARY | Unauthenticated | Downloaded 10/27/26 06:31 PM UTC

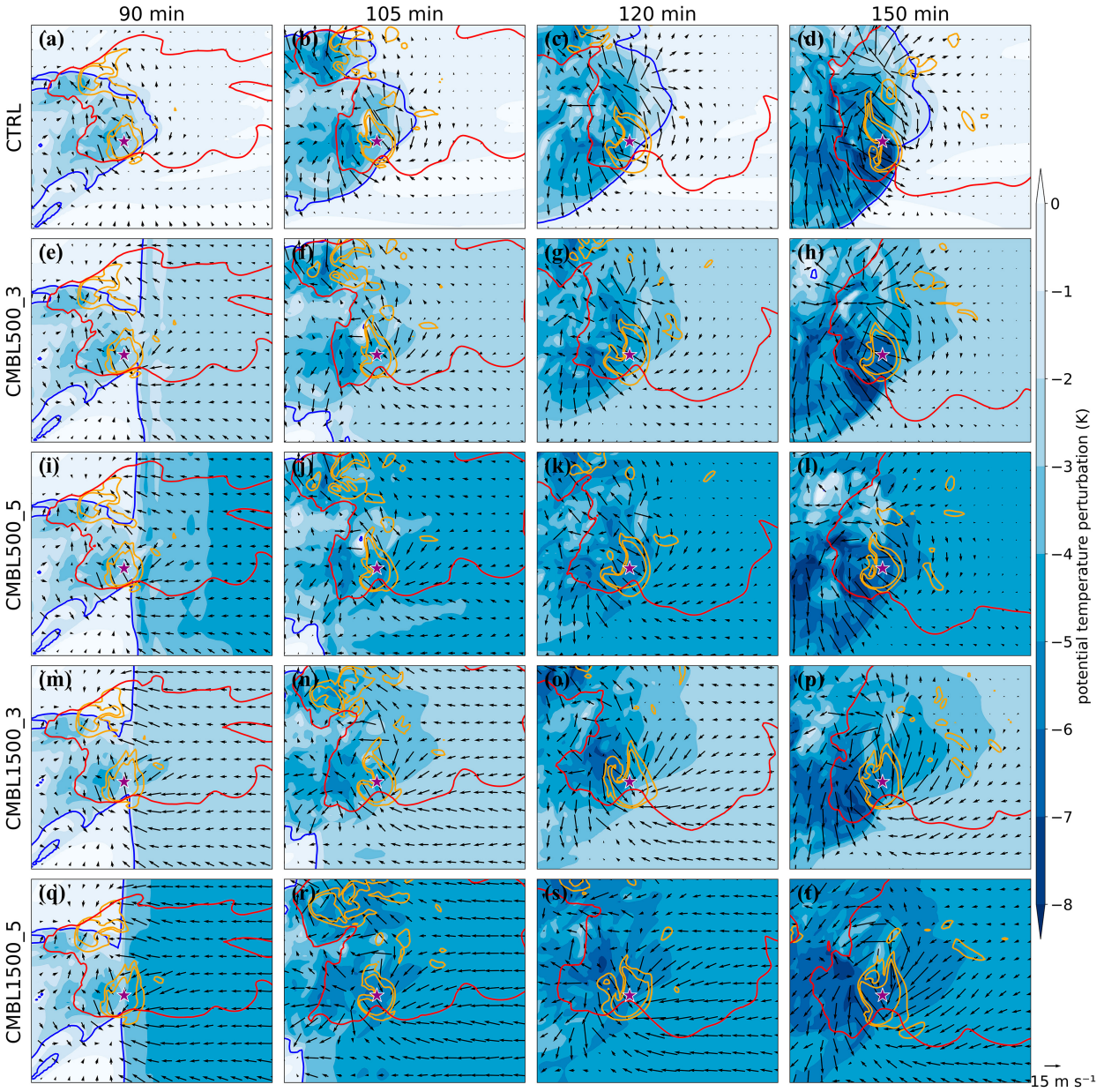


FIG. 12. Evolution of the cold pool for (first row) CTRL, (second row) CMBL500_3, (third row) CMBL500_5, (fourth row) CMBL1500_3, and (fifth row) CMBL1500_5. Filled contours (potential temperature perturbation), wind vectors, red contour lines (20 dBZ), and blue contour lines (-0.05 m s^{-2} buoyancy) depict fields at the lowest model level above ground (50 m). The reference vector is located at the bottom-right corner. Orange contour lines represent vertical velocity (~6 km) of 5 and 15 m s^{-1}. The purple star denotes the right-moving storm center.

gust front and allowing more near-surface cool air to be drawn into the updraft. However, the case is different for the 500-m CMBL. Despite the cold pool being substantially stronger than the 500-m CMBL after 120 min (Figs. 12e–l), the colder CMBL air is scarcely lifted into the updraft (Figs. 11d–i). This occurs because, beyond the lifting provided by the gust front, DVPPGF also enhances the updraft's capacity to ingest stable air.

As shown in Fig. 12, the surface winds ahead of the storm gust front and the sea-breeze flows differ significantly between the h = 500 m and h = 1500 m runs. The winds toward the gust front are much stronger in the h = 1500 m cases (Figs. 12m–t), and they are even stronger in the CMBL1500_5 run. These strong surface winds are clearly the result of the forward surging of the CMBL flows, and the deeper and colder the CMBL is, the stronger the surging winds are. In the early stage (90–140 min), the westward-moving sea-breeze air collides with the cold pool, contributing to stronger convergence along the gust front. The stronger near-surface convergence/deformation creates larger

Brought to you by UNIVERSITY OF OKLAHOMA LIBRARY | Unauthenticated | Downloaded 10/27/26 06:31 PM UTC

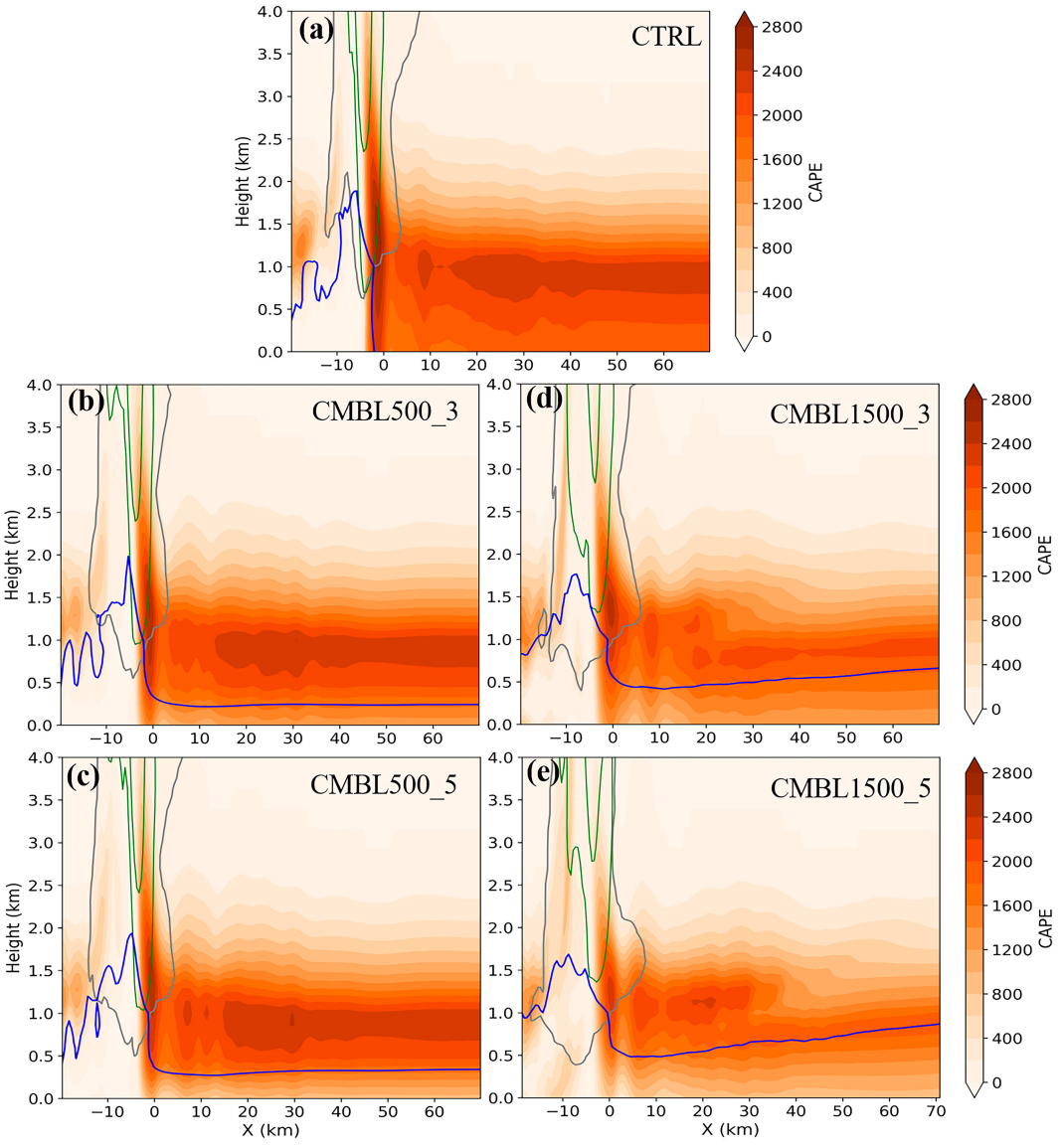


FIG. 13. Vertical cross sections at 120 min for (a) CTRL, (b) CMBL500_3, (c) CMBL500_5, (d) CMBL1500_3, and (e) CMBL1500_5. Contour lines are as in Fig. 11. Filled contours represent CAPE. The east–west vertical cross sections are taken from west to east through the storm center with values averaged over a width of 5 km in the north–south direction.

positive pressure perturbations in the first stage that may reduce downward TDVPPGF. The increased low-level shear and SRH also increase the rotation of the mesocyclone (through the spin term) during the later stage (140–180 min), which helps increase the upward NDVPPGF from decreased perturbation pressure at the mesocyclone levels. With such dynamic effects, cold near-surface air parcels from within the CMBL can be lifted and enter the deep updrafts (Fig. 11), creating stronger and wider updrafts at the lower–mid levels and more precipitation (cf. Fig. 5) even though the buoyancy of the updrafts is lower (Fig. 8b). Such effects are most pronounced in the CMBL1500_5 case. The differing ability to ingest cold air between the 1500-m CMBL and the 500-m CMBL is one contributing factor to the lower buoyant accelerations observed at 1500 m compared to 500 m (Fig. 8b). At 120 min, more parcels are lifted above 6 km by the updraft in the $h = 500$ m cases than in the $h = 1500$ m cases (Figs. 11f,i,l,o). This is because, given identical parcel release locations ($x = -50$ to 0 km) at 60 min, the supercell updraft in the $h = 1500$ m cases ingests parcels more rapidly and in greater numbers above the CMBL during the early stage, leaving fewer initially released parcels available to be subsequently lifted into updraft.

In addition to differences in the temporal evolutions of ingested parcel heights observed within the CMBL simulations, intersimulation differences are also evident between the CTRL and CMBL simulations for parcels ingested at the same times. Figure 13 illustrates the differences in the initial positions of

Brought to you by UNIVERSITY OF OKLAHOMA LIBRARY | Unauthenticated | Downloaded 10/27/26 06:31 PM UTC

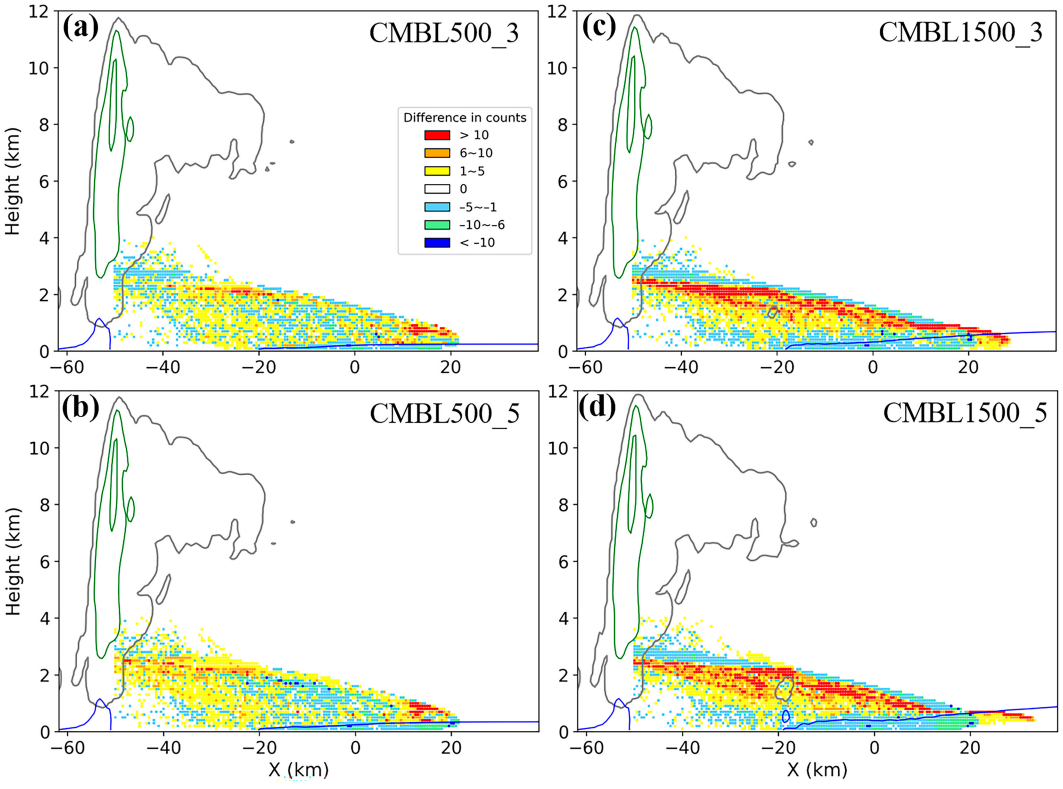


FIG. 14. Vertical cross sections at 60 min for (a) CMBL500_3, (b) CMBL500_5, (c) CMBL1500_3, and (d) CMBL1500_5. Contour lines are as in Fig. 11. Colored dots indicate the difference in the number of parcels at 60 min that end up in midlevel updraft at 150 min between CMBL and CTRL simulations. Warm colored dots represent locations where more parcels are ingested into the updraft in CMBL than in CTRL, whereas cool colored dots indicate otherwise. Cross sections are taken from west to east through the storm center with values averaged over a width of 5 km.

parcels ingested into the midlevel updraft at 150 min or the mature stage of supercell between the CMBL and CTRL experiments, providing an intuitive view of how sea-breeze flows influence parcel characteristics. There are no significant height differences between the h = 500-m CMBL experiments and CTRL. Slightly more elevated parcels located ahead of the sea-breeze front are ingested in the 500-m CMBL simulations. Fewer parcels within the CMBL layer are ingested by the updraft, as found earlier, while parcels above the CMBL layer (at $x > -20$ km) exhibit generally similar positional characteristics between the h = 500-m CMBL simulations and CTRL. These results are consistent with earlier findings: The shallow CMBL and resulting sea-breeze flows produce relatively small impacts on the simulated supercell and its circulations. However, in the h = 1500-m CMBL simulations, the stronger and wider lower-level updraft draws in significantly more elevated parcels from above the CMBL, as indicated by the many yellow and red dots in Figs. 14c and 14d. In addition, more parcels within the CMBL layer at $x > 20$ km are ingested in the 1500-m CMBL, which should be attributed to the accelerated inflow into the storm, hence more distant parcels being ingested. There are also fewer parcels ingested from within the CMBL layer in general compared to CTRL, although some of the parcels are indeed ingested, as seen earlier in Fig. 11.

The vertical cross sections of air parcel CAPE at different levels at 120 min provide insight into the thermodynamic differences between the CMBL and CTRL simulations (Fig. 15). In CTRL that is not affected by the CMBL air, a layer of relatively large CAPE of over 2200 J kg^{-1} is found near the 1 km AGL, which is the most unstable layer in the base-state sounding (Fig. 15a). In CMBL500_3 and CMBL500_5, this most unstable layer is not much affected, with the main difference being with the reduced CAPE within the CMBL. In CMBL1500_3 and CMBL1500_5, the deep initial CMBL clearly caused the erosion of the low-level CAPE, reducing the maximum CAPE upstream. Close to the storm at $x < 30$ km, larger values of CAPE are elevated, apparently uplifted by the flow convergence. The most unstable CAPE is still above 2000 J kg^{-1}, which can still support the development of rigorous updrafts. The reduction in the maximum CAPE in deep CMBL cases compared to CTRL and the shallow CMBL cases is more than compensated by the increase in dynamic forcing, as discussed earlier.

f. *Sensitivity to CAPE profile*

In the earlier CMBL air intrusion experiments, the supercell draws in a large number of elevated parcels with the aid of the strong sea-breeze flows in the deep CMBL cases. With the sounding profile used in those experiments, the maximum

Brought to you by UNIVERSITY OF OKLAHOMA LIBRARY | Unauthenticated | Downloaded 10/27/26 06:31 PM UTC

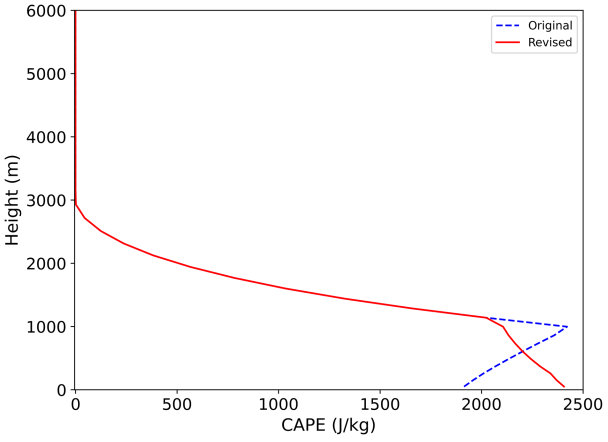


FIG. 15. The vertical profile of original CAPE (blue dashed line) and revised CAPE (red solid line).

CAPE is actually located at ~1-km level, as shown by the dashed line in Fig. 15, and such, a CAPE profile arises from the constant moisture mixing ratio specified in the ~1-km deep boundary layer (Fig. 1) in the analytic sounding of Weisman and Klemp (1982). The elevated parcels drawn into the storm therefore possess no smaller CAPE than air parcels from lower levels. Such a CAPE profile might have contributed to the fact that the introduction of CMBL air into the inflow is not detrimental to the supercell storm development. It is therefore natural to ask if the storm response can be different if the maximum CAPE is located near the surface. To test the sensitivity of the supercell response to the CAPE profile, a modified sounding is used in which moisture is adjusted to produce a surface-based CAPE maximum, as shown by the red curve in Fig. 15. Five new simulations, named CTRLr, CMBL500_3r, CMBL500_5r, CMBL1500_3r, and CMBL1500_5r, with "r" indicating "revised," are conducted using the revised sounding, while all other configurations remain the same.

Interestingly, the overall responses of the simulated storms to the cold-air intrusion are similar to the original CAPE profile case (cf. Figs. 16 and 5). The strength of supercell mesocyclone does not decrease but increases in $h = 1500$ m CMBLr runs compared to CTRLr in terms of the vertical vorticity below 4-km level (e.g., ~0.018 s^{-1} in CMBL1500_3r, ~0.022 s^{-1} in CMBL1500_5r, and 0.016 in CTRLr at 3 km; Fig. 16b), and the increase is slightly more pronounced than the original sounding cases (cf. Fig. 5b). The strong updraft areas (e.g., ~54 m^2 in CMBL1500_3, ~61 m^2 in CMBL1500_5, and ~45 m^2 in CTRL at 6 km; Fig. 16c) and condensate masses (e.g., with maximum values of ~7×10^7 kg in $h = 1500$ m runs and ~5×10^7 kg in CTRL; Fig. 16d) in the $h = 1500$ m runs are also noticeably higher throughout the storm depth compared to CTRLr, while the midlevel updraft velocity (~42 m s^{-1} in CMBL1500_3, ~39 m s^{-1} in CMBL1500_5, and ~43 m s^{-1} in CTRL at 6 km; Fig. 16a) and vertical vorticity (~0.041 s^{-1} in CMBL1500_3, ~0.038 s^{-1} in CMBL1500_5, and ~0.044 s^{-1} in CTRL at 6 km; Fig. 16b) are weaker, as in the original sounding cases. In contrast, the midlevel vertical vorticity of 500-m CMBL (~0.043 s^{-1}) in the revised simulations is less than that in CTRLr (~0.045 s^{-1}; Fig. 16b), different from the original sounding cases (Fig. 5b). Comparing CTRLr and CTRL, all parameters shown are somewhat larger between the 4- and 8-km levels in CTRLr (Figs. 16 and 5). Apparently, with the revised CAPE profile, the moister near-surface air (see Fig. 1) is helping to produce stronger and larger updrafts and more condensate mass in CTRLr. With a stronger supercell in CTRL, the dynamic responses (such as the lower-level mesocyclone intensity) to the strong deep CMBL air intrusion, as discussed earlier, are apparently also stronger.

As in the original CAPE profile cases, vertical cross sections of CAPE at 120 min from the five revised simulations are shown in Fig. 17. They help explain the changes discussed above. With the revised CAPE profile, the maximum CAPE of the inflow in CTRLr now occurs at the surface and the original maximum gust-front lifting has shifted from being elevated to near the surface (Fig. 17a). This explains why the strong updraft area at ~2-km height is increased from the ~7 km^2 in CTRL (Fig. 5c) to about ~15 km^2 in CTRLr (Fig. 16c). In the $h = 500$ m CMBLr cases (Figs. 17b,c), the elevated maximum CAPE exhibits a reduction of about 200 J kg^{-1} relative to the original $h = 500$ m CMBL cases (Figs. 13b,c), which leads to a weaker lower-level mesocyclone. In the 1500-m CMBLr simulations, the elevated maximum CAPE (Figs. 17d,e) is similar to that in the original CAPE profile cases (Figs. 13d,e). Actually, the maximum CAPE at ~1-km level in CMBL1500_5r is even greater than that in CTRLr, specially at earlier times (Fig. 18). Figure 18 shows that CAPE larger than 2200 J kg^{-1} is found in the 500–1000-m layer in CMBL1500_5r between 60 and 100 min (lower panels in Fig. 18), while that in CTRLr is all below 2200 J kg^{-1} (upper panels of Fig. 18). Clearly, in CMBL1500_5r, the strong sea breeze effectively lifts air with large CAPE from the 0- to 500-m layer to above 500 m. As the sea-breeze front advances toward the cold pool, more of the elevated air parcels that have been displaced upward to such levels are fed into the updraft. All of the above results show that even with an environmental sounding whose CAPE maximum is at the surface, so that more of the large near-surface CAPE in the inflow is replaced by the deep cold CMBL air with lower CAPE, the simulated supercell storm can still be stronger in terms of low-level updraft area, intensity, rotation, and precipitation, due to dynamic responses, and such responses can be even stronger in the case of a stronger control storm simulation.

4. Conclusions

Despite their potential to produce large hail, damaging winds, intense rainfall, and even tornadoes (Soderholm et al. 2017; Jin et al. 2019; Chan et al. 2022), coastal supercell thunderstorms that are affected by commonly occurring sea-breeze flows in coastal regions have received relatively little attention in previous studies. Idealized simulations of a supercell storm are performed, in which cold sea-breeze flows driven by a specified pool of CMBL air of different depths and coldness intrude into the supercell storm inflow and are compared to a

Brought to you by UNIVERSITY OF OKLAHOMA LIBRARY | Unauthenticated | Downloaded 10/27/26 06:31 PM UTC

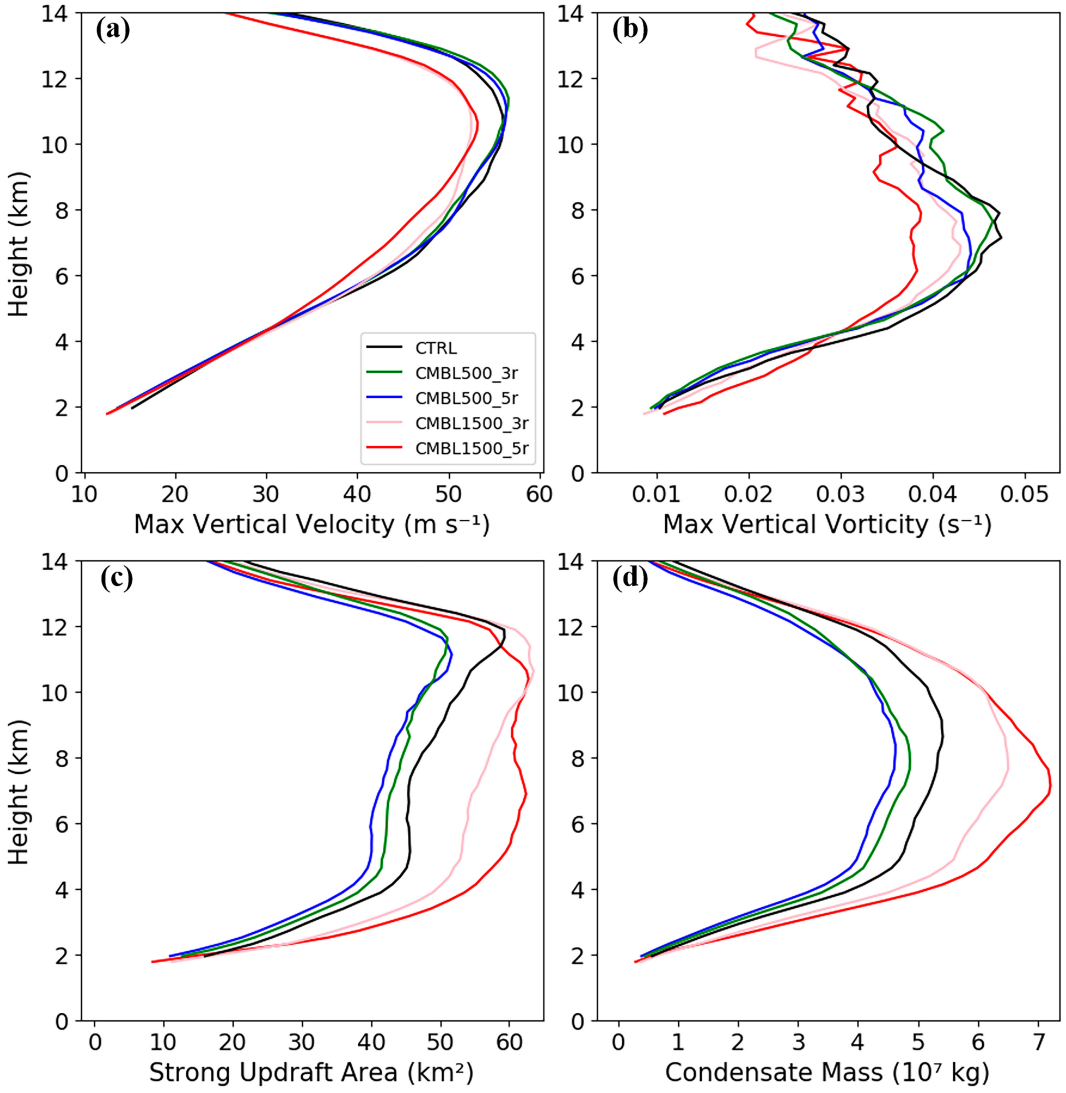


FIG. 16. As in Fig. 5, but for simulations with revised CAPE profile.

CTRL simulation without the sea-breeze flow intrusion. The four sea-breeze simulations have a CMBL with an initial maximum perturbation potential temperature of −3 or −5 K and an initial depth h = 500 m (shallow CMBL cases) or 1500 m (deep CMBL cases), respectively.

The simulated supercell's response to the intrusion of sea-breeze flows is more strongly influenced by the depth of the CMBL than by the magnitude of its negative potential temperature perturbation. The CMBL air creates strong low-level westward-moving flows as well as a local temperature deficit; in the meantime, it alters the 0–1-km shear and SRH and surface-based CAPE in the storm inflow region. As time progresses, the deep CMBL cases produce significantly enhanced low-level shear within the storm inflow region, while low-level shear in the shallow CMBL cases is just marginally larger than that in CTRL. The 0–1-km SRH only noticeably increases in the later stage, and it is most evident in CMBL1500_5. All simulations exhibit similar maximum updraft velocities below the 4-km level, while deep CMBL cases show larger maximum vertical vorticities than CTRL at the same levels. Above the 6-km level, vertical velocity and vorticity in deep CMBL cases decrease markedly compared to CTRL. The updraft condensate mass for deep CMBL cases is much more than that of CTRL at all altitudes, which is highly correlated with the updraft area (CMBL1500_5 has the largest updraft area), which is intuitively surprising, given the coldness of the intruding sea-breeze air.

After starting to collide with the cold pool at ~90 min, the influence of the sea-breeze flows is divided into two stages: the early stage (90–140 min) and the later stage (140–180 min). In the early stage, the sea-breeze flows increase significantly in crosswise vorticity below 500 m, but the storm-relative velocity over 0–1 km is larger. Therefore, the 0–1-km SRH in CMBL simulations is still slightly larger than that in CTRL. The

Brought to you by UNIVERSITY OF OKLAHOMA LIBRARY | Unauthenticated | Downloaded 10/27/26 06:31 PM UTC

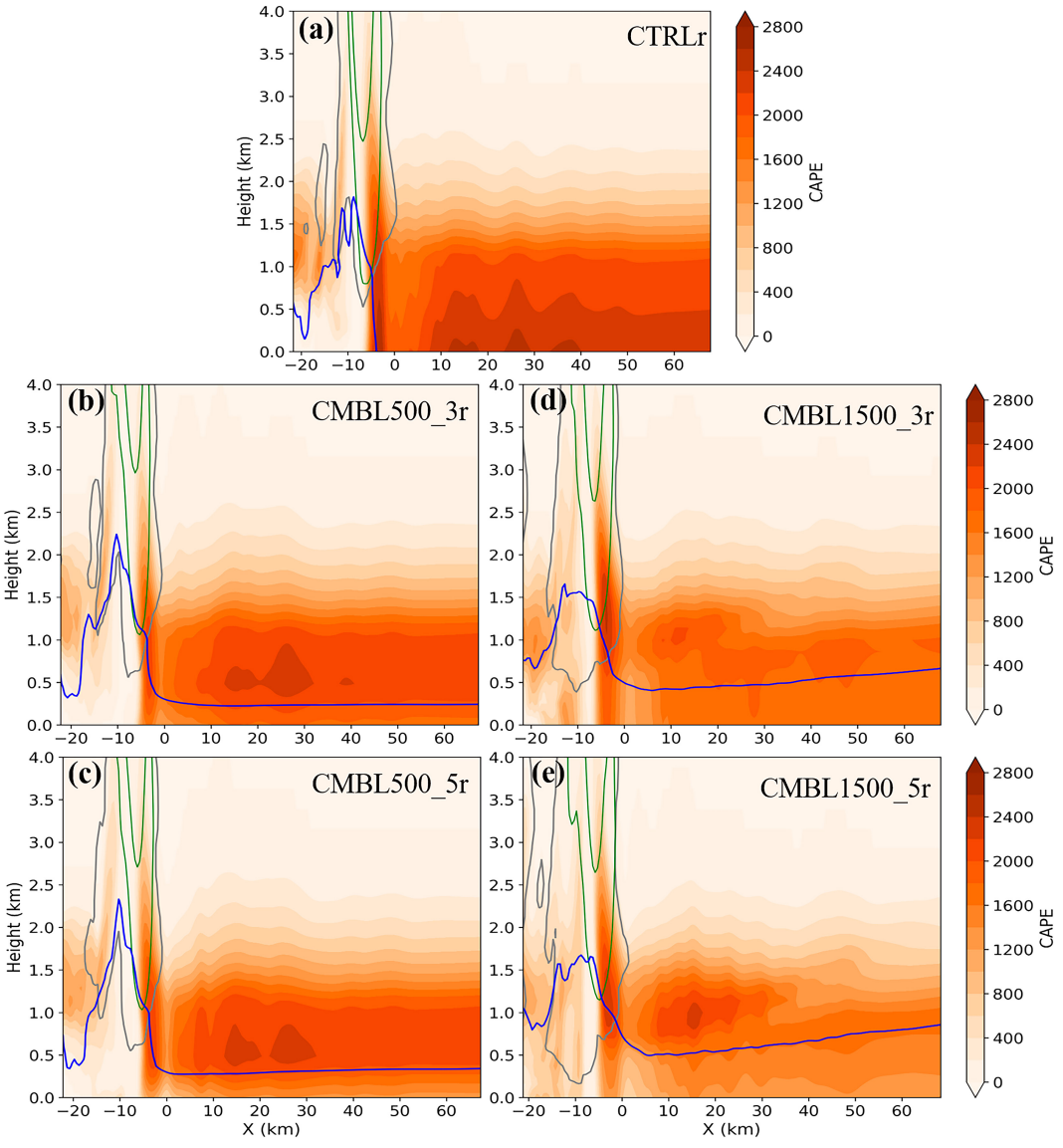


FIG. 17. As in Fig. 15, but for simulations with revised CAPE profile.

updrafts in deep CMBL cases are weaker than those in CTRL during the first stage; apparently, the increase in the 0–1-km SRH is not enough to compensate for the cold CMBL effect on updraft buoyancy. In the later stage, the strong flows behind the sea-breeze front make the horizontal vorticity more aligned with the storm-relative flow, causing a large increase in 0–1-km SRH and 2–5-km updraft helicity in deep CMBL cases and hence stronger updrafts and heavier precipitation.

Sea-breeze flows clearly enhance the DVPPGF below 4 km within the supercell updraft, and this positive effect is strongest in the deep CMBL cases. Conversely, EB in deep CMBL cases is consistently lower throughout the depth due to decreased CAPE. In deep CMBL cases, persistently lower EB leads to a weakened midlevel updraft, resulting in reduced DVPPGF above the midlevel. As updrafts in the shallow CMBL cases are less affected by the negative thermal effect, the EB shows only slight reductions relative to CTRL at certain altitudes.

While sea-breeze flows can strengthen the low-level DVPPGF in updrafts, the precise process by which this occurs is not yet understood. DVPPGF can be decomposed into convergence-/deformation-induced TDVPPGF and rotation-induced NDVPPGF. Through convergence/deformation, the eastward-moving deep-sea-breeze front strengthens positive TDVPPGF near the gust-front level and diminishes downward TDVPPGF within the updraft, leading to an increase in low-level DVPPGF during the early stage. During the later stage, significantly enhanced 0–1-km SRH and a strengthened updraft in deep CMBL cases facilitate upward NDVPPGF by lowering the perturbation pressure near the mesocyclone level.

Air parcels in the vicinity of the sea-breeze air are released to explore why differences in updraft area arise between

Brought to you by UNIVERSITY OF OKLAHOMA LIBRARY | Unauthenticated | Downloaded 10/27/26 06:31 PM UTC

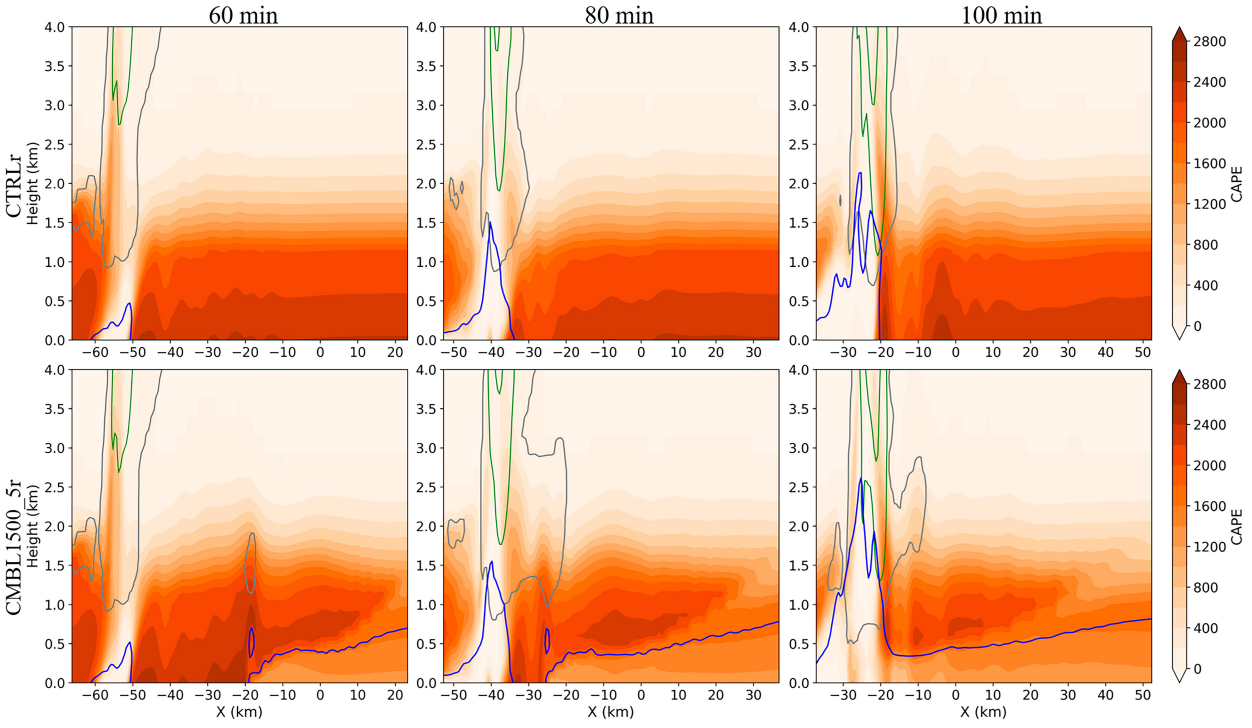


FIG. 18. As in Fig. 15, but for CTRLr and CMBL1500_5r simulations of revised CAPE profile at 60, 80, and 100 min.

CTRL and coastal simulations. Consistent with previous stable intrusion storm studies (e.g., Davenport and Parker 2015), cooler air within CMBL cannot be ingested into updraft in most CMBL simulations. However, this phenomenon does not occur in deep CMBL cases during subsequent stages. The ability to ingest CMBL air is related to the cold-pool-induced gust-front lifting and DVPPGF. When the supercell develops into the mature stage, the cold pool becomes much colder than the CMBL air and has enhanced gust-front lifting. In addition, the larger low-level DVPPGF induced by the deep-sea-breeze flows (TDVPPGF in the early stage and NDVPPGF in the later stage) in CMBL1500 also contributes to this effect, while its absence in shallow marine atmospheric boundary layer (MABL) cases helps explain why the updraft is unable to ingest air below the CMBL level. Though ingesting reduced-CAPE air into the updraft weakens midlevel maximum vertical velocity and vorticity and reduces EB within the updraft, the positive DVPPGF effect induced by the deep-sea-breeze flows can compensate for this negative thermal effect. As a result, the updraft in deep CMBL cases draws substantially more parcels from elevated and some surface regions, leading to larger areas of strong updraft, greater total condensate mass, and increased precipitation.

Updraft in deep CMBL cases relies on elevated parcels, and the base sounding used happens to have its CAPE maximum located aloft rather than at the surface, which is beneficial to lift elevated parcels to updraft (although the CAPE in deep CMBL cases is still lower than in CTRL). Simulations with sounding characterized by maximum CAPE shifts from elevated layers to the surface are conducted to test the sensitivity of CMBL-related effects to the CAPE profile. Results show that the deep CMBL air acts like a cold front, lifting high-CAPE air aloft and producing a CAPE distribution similar to that in the original simulations. In consequence, the condensate mass or updraft area in deep CMBL cases is still larger than that in CTRL.

The experiments presented in this study used 500-m horizontal grid spacing and vertically stretched grid spacing, with a vertical resolution of approximately 100 m below 1 km, which may be low for simulating detailed sea-breeze and storm outflow interactions. To assess the sensitivity to the spatial resolutions, we repeated the simulations with 250-m horizontal grid spacing and a stretched vertical grid with 50-m grid spacing below 3 km during the paper review process and performed the same set of analyses on the higher-resolution simulation data. Below the level of 4 km, all simulations exhibit similar vertical velocities ($\sim$20 m s^{-1} at 3 km), and the maximum vertical vorticities in CMBL1500_3 ($\sim$0.028 s^{-1} at 3 km) and CMBL1500_5 ($\sim$0.034 s^{-1} at 3 km) are still stronger than in CTRL ($\sim$0.021 s^{-1} at 3 km). Above 6 km, both vertical velocity and vorticity in h = 1500 m simulations (vertical velocity $\sim$ 51 m s^{-1} and vorticity $\sim$ 0.075 s^{-1} in CMBL1500_3; $\sim$51 m s^{-1} and $\sim$0.068 s^{-1} in CMBL1500_5 at 8 km) remain weaker than those in CTRL ($\sim$54 m s^{-1} and $\sim$0.080 s^{-1} at 8 km). In addition, the updraft characteristics in h = 500 m are still similar to those in CTRL. The magnitudes of vertical velocity and vorticity within updrafts are larger in the higher-resolution simulation, which may be associated with better-resolved turbulent processes that contribute to storm development. Although differences exist in the details

Brought to you by UNIVERSITY OF OKLAHOMA LIBRARY | Unauthenticated | Downloaded 10/27/26 06:31 PM UTC

between the lower- and higher-resolution simulations, the overall conclusions regarding the dynamical and thermodynamical responses of sea-breeze flow on supercells remain unchanged.

Given the highly idealized nature of the simulations and the limited parameter space explored, further work is needed to determine the broader applicability of the conclusions presented here. The sounding used in this study is idealized and may not fully represent coastal environments. Future work should examine additional realistic soundings representative of coastal supercell environments as well as different CMBL depths and intensities to further assess the generality of the results presented here. This work primarily focuses on the influence of sea-breeze flow on supercells in the mature stage, and future work should also examine the impact of supercells in the earlier development and later dissipation stages. Of course, studies on supercells and sea-breeze fronts in realistic settings, with real data initiation, are also worthwhile and will more directly help with prediction of such phenomena. Observational studies, including climatological studies, should also be carried out. In addition, the sensitivity of storm–sea-breeze interactions to different shoreline orientations relative to storm motion and environmental shear vectors should be examined. Furthermore, this study does not account for inland boundary layer heterogeneity, including organized boundary layer structures such as horizontal convective rolls and open or closed cellular convection, nor for the full three-dimensional structure of the sea-breeze front. These processes may influence storm–sea-breeze interactions and warrant further investigation.

Acknowledgments. This project was primarily supported by NSFC Grant 42588101. The authors thank Dr. Shizuo Fu for providing a stand-alone pressure decomposition code used in this study.

Data availability statement. The data used in this paper can be found at Harvard Dataverse at https://doi.org/10.7910/DVN/L4ZYIX.

REFERENCES

Alfaro, D. A., 2017: Low-tropospheric shear in the structure of squall lines: Impacts on latent heating under layer-lifting ascent. *J. Atmos. Sci.*, **74**, 229–248, https://doi.org/10.1175/JAS-D-16-0168.1.

Bergemann, M., C. Jakob, and T. P. Lane, 2015: Global detection and analysis of coastline-associated rainfall using an objective pattern recognition technique. *J. Climate*, **28**, 7225–7236, https://doi.org/10.1175/JCLI-D-15-0098.1.

Billings, J. M., and M. D. Parker, 2012: Evolution and maintenance of the 22–23 June 2003 nocturnal convection during BAMEX. *Wea. Forecasting*, **27**, 279–300, https://doi.org/10.1175/WAF-D-11-00056.1.

Boyer, C. H., J. M. Keeler, and B. C. Rakoczy, 2025: An idealized parameter study of destabilization and convection initiation in coastal regions. Part I: Calm or offshore synoptic-scale flow. *J. Atmos. Sci.*, **82**, 519–539, https://doi.org/10.1175/JAS-D-23-0180.1.

Bryan, G. H., and J. M. Fritsch, 2002: A benchmark simulation for moist nonhydrostatic numerical models. *Mon. Wea. Rev.*, **130**, 2917–2928, https://doi.org/10.1175/1520-0493(2002)130<2917:ABSFMN>2.0.CO;2.

Chan, P. W., K. K. Hon, P. Robinson, K. Kosiba, J. Wurman, and Q. S. Li, 2022: Analysis and numerical simulation of a supercell tornado at the Hong Kong adjacent waters. *Meteor. Appl.*, **29**, e2056, https://doi.org/10.1002/met.2056.

Chen, G., H. Iwai, S. Ishii, K. Saito, H. Seko, W. Sha, and T. Iwasaki, 2019: Structures of the sea-breeze front in dual-Doppler lidar observation and coupled mesoscale-to-LES modeling. *J. Geophys. Res. Atmos.*, **124**, 2397–2413, https://doi.org/10.1029/2018JD029017.

Chen, X., F. Zhang, and K. Zhao, 2016: Diurnal variations of the land–sea breeze and its related precipitation over South China. *J. Atmos. Sci.*, **73**, 4793–4815, https://doi.org/10.1175/JAS-D-16-0106.1.

Coffer, B. E., and M. D. Parker, 2015: Impacts of increasing low-level shear on supercells during the early evening transition. *Mon. Wea. Rev.*, **143**, 1945–1969, https://doi.org/10.1175/MWR-D-14-00328.1.

——, M. Taszarek, and M. D. Parker, 2020: Near-ground wind profiles of tornadic and nontornadic environments in the United States and Europe from ERA5 reanalyses. *Wea. Forecasting*, **35**, 2621–2638, https://doi.org/10.1175/WAF-D-20-0153.1.

Dailey, P. S., and R. G. Fovell, 1999: Numerical simulation of the interaction between the sea-breeze front and horizontal convective rolls. Part I: Offshore ambient flow. *Mon. Wea. Rev.*, **127**, 858–878, https://doi.org/10.1175/1520-0493(1999)127<0858:NSOTIB>2.0.CO;2.

Davenport, C. E., and M. D. Parker, 2015: Impact of environmental heterogeneity on the dynamics of a dissipating supercell thunderstorm. *Mon. Wea. Rev.*, **143**, 4244–4277, https://doi.org/10.1175/MWR-D-15-0072.1.

Doswell, C. A., III, and P. M. Markowski, 2004: Is buoyancy a relative quantity? *Mon. Wea. Rev.*, **132**, 853–863, https://doi.org/10.1175/1520-0493(2004)132<0853:IBARQ>2.0.CO;2.

Fu, S., R. Rotunno, and H. Xue, 2022: Convective updrafts near sea-breeze fronts. *Atmos. Chem. Phys.*, **22**, 7727–7738, https://doi.org/10.5194/acp-22-7727-2022.

Hartigan, J., R. A. Warren, J. S. Soderholm, and H. Richter, 2021: Simulated changes in storm morphology associated with a sea-breeze air mass. *Mon. Wea. Rev.*, **149**, 333–351, https://doi.org/10.1175/MWR-D-20-0069.1.

Huang, W., and M. Xue, 2025: What forces the rapid vertical acceleration and vorticity intensification near ground in tornadoes? Diagnostic analysis based on a numerically simulated real tornado. *J. Atmos. Sci.*, **82**, 2541–2568, https://doi.org/10.1175/JAS-D-25-0033.1.

Jin, Z., X. Yi, X. Sun, Y. Liu, and G. Li, 2019: Analysis of heavy precipitation supercell environment condition and structure in Tianjin coastal area (in Chinese with English abstract). *Torrential Rain Disasters*, **38**, 606–614, https://doi.org/10.3969/j.issn.1004-9045.2019.06.005.

Lombardo, K., and B. A. Colle, 2013: Processes controlling the structure and longevity of two quasi-linear convective systems crossing the southern New England coast. *Mon. Wea. Rev.*, **141**, 3710–3734, https://doi.org/10.1175/MWR-D-12-00336.1.

——, and T. Kading, 2018: The behavior of squall lines in horizontally heterogeneous coastal environments. *J. Atmos. Sci.*, **75**, 1243–1269, https://doi.org/10.1175/JAS-D-17-0248.1.

Brought to you by UNIVERSITY OF OKLAHOMA LIBRARY | Unauthenticated | Downloaded 10/27/26 06:31 PM UTC

——, E. Sinsky, Y. Jia, M. M. Whitney, and J. Edson, 2016: Sensitivity of simulated sea breezes to initial conditions in complex coastal regions. *Mon. Wea. Rev.*, **144**, 1299–1320, https://doi.org/10.1175/MWR-D-15-0306.1.

Markowski, P., and Y. Richardson, 2010: Hazards associated with deep moist convection. *Mesoscale Meteorology in Midlatitudes*, John Wiley and Sons, 273–313.

——, ——, E. Rasmussen, J. Straka, R. Davies-Jones, and R. J. Trapp, 2008: Vortex lines within low-level mesocyclones obtained from pseudo-dual-Doppler radar observations. *Mon. Wea. Rev.*, **136**, 3513–3535, https://doi.org/10.1175/2008MWR2315.1.

McCaul, E. W., Jr., and C. Cohen, 2002: The impact on simulated storm structure and intensity of variations in the mixed layer and moist layer depths. *Mon. Wea. Rev.*, **130**, 1722–1748, https://doi.org/10.1175/1520-0493(2002)130<1722:TIOSSS>2.0.CO;2.

Meng, Z., and Coauthors, 2018: The deadliest tornado (EF4) in the past 40 years in China. *Wea. Forecasting*, **33**, 693–713, https://doi.org/10.1175/WAF-D-17-0085.1.

Morrison, H., G. Thompson, and V. Tatarskii, 2009: Impact of cloud microphysics on the development of trailing stratiform-precipitation in a simulated squall line: Comparison of one- and two-moment schemes. *Mon. Wea. Rev.*, **137**, 991–1007, https://doi.org/10.1175/2008MWR2556.1.

Parker, M. D., 2008: Response of simulated squall lines to low-level cooling. *J. Atmos. Sci.*, **65**, 1323–1341, https://doi.org/10.1175/2007JAS2507.1.

Riggin, R. R., IV, C. E. Davenport, M. D. Eastin, K. E. McKeown, S. M. Purpura, and B. T. Katona, 2025: Idealized simulations of supercell thunderstorms traversing the Appalachian Mountains. *Mon. Wea. Rev.*, **153**, 373–402, https://doi.org/10.1175/MWR-D-23-0285.1.

Rotunno, R., J. B. Klemp, and M. L. Weisman, 1988: A theory for strong, long-lived squall lines. *J. Atmos. Sci.*, **45**, 463–485, https://doi.org/10.1175/1520-0469(1988)045<0463:ATFSLL>2.0.CO;2.

Soderholm, J. S., H. A. McGowan, H. Richter, K. Walsh, T. Wedd, and T. M. Weckwerth, 2017: Diurnal preconditioning of subtropical coastal convective storm environments. *Mon. Wea. Rev.*, **145**, 3839–3859, https://doi.org/10.1175/MWR-D-16-0330.1.

Sun, Z., M. Xue, K. Zhu, and B. Zhou, 2019: Prediction of an EF4 supercell tornado in Funing, China: Resolution dependency of simulated tornadoes and their structures. *Atmos. Res.*, **229**, 175–189, https://doi.org/10.1016/j.atmosres.2019.06.019.

United Nations, 2017: Factsheet: People and oceans. 2 pp., https://sustainabledevelopment.un.org/content/documents/Ocean_Factsheet_People.pdf.

Warren, R. A., H. Richter, H. A. Ramsay, S. T. Siems, and M. J. Manton, 2017: Impact of variations in upper-level shear on simulated supercells. *Mon. Wea. Rev.*, **145**, 2659–2681, https://doi.org/10.1175/MWR-D-16-0412.1.

Weisman, M. L., and J. B. Klemp, 1982: The dependence of numerically simulated convective storms on vertical wind shear and buoyancy. *Mon. Wea. Rev.*, **110**, 504–520, https://doi.org/10.1175/1520-0493(1982)110<0504:TDONSC>2.0.CO;2.

——, ——, and R. Rotunno, 1988: Structure and evolution of numerically simulated squall lines. *J. Atmos. Sci.*, **45**, 1990–2013, https://doi.org/10.1175/1520-0469(1988)045<1990:SAEONS>2.0.CO;2.

Wicker, L. J., and W. C. Skamarock, 2002: Time-splitting methods for elastic models using forward time schemes. *Mon. Wea. Rev.*, **130**, 2088–2097, https://doi.org/10.1175/1520-0493(2002)130<2088:TSMFEM>2.0.CO;2.

Wissmeier, U., R. K. Smith, and R. Goler, 2010: The formation of a multicell thunderstorm behind a sea-breeze front. *Quart. J. Roy. Meteor. Soc.*, **136**, 2176–2188, https://doi.org/10.1002/qj.691.

Wu, F., and K. Lombardo, 2024: Sensitivity of coastal squall-line evolution to numerical sea-breeze initialization method. *J. Atmos. Sci.*, **81**, 1289–1321, https://doi.org/10.1175/JAS-D-23-0174.1.

Yu, C.-K., and Y.-H. Hsieh, 2009: Formation of the convective lines off the mountainous coast of southeastern Taiwan: A case study of 3 January 2004. *Mon. Wea. Rev.*, **137**, 3072–3091, https://doi.org/10.1175/2009MWR2867.1.

Zhang, C., M. Xue, K. Zhu, and X. Yu, 2023: Climatology of significant tornadoes within China and comparison of tornado environments between the United States and China. *Mon. Wea. Rev.*, **151**, 465–484, https://doi.org/10.1175/MWR-D-22-0070.1.

Zhang, R., M. Xue, and X. Yu, 2025: Environments of tornadic and non-tornadic supercells in China and optimized significant tornado parameter for China region. *Quart. J. Roy. Meteor. Soc.*, **151**, e5027, https://doi.org/10.1002/qj.5027.

Brought to you by UNIVERSITY OF OKLAHOMA LIBRARY | Unauthenticated | Downloaded 10/27/26 06:31 PM UTC